

ILLUMINATING THE CHEMO-MECHANICS OF
ENVIRONMENT ASSISTED FATIGUE IN
ALUMINUM

A Dissertation

Presented to the Faculty of the Graduate School
of Cornell University

in Partial Fulfillment of the Requirements for the Degree of
Doctor of Philosophy

by

Richard J. Zamora

January 2015

© 2015 Richard J. Zamora
ALL RIGHTS RESERVED

ILLUMINATING THE CHEMO-MECHANICS OF ENVIRONMENT
ASSISTED FATIGUE IN ALUMINUM

Richard J. Zamora, Ph.D.

Cornell University 2015

This dissertation composes three papers detailing work intended to illuminate the atomistic-scale mechanisms governing environment assisted fatigue crack growth in aluminum. All studies focus on the application of concurrent atomistic-continuum multiscale modeling, utilizing the coupled atomistic and discrete dislocation (CADD) methodology. First, an ab-initio prediction of environmental embrittlement in aluminum is demonstrated using a density functional theory (DFT) based multiscale framework to simulate the behavior of a loaded crack-tip in the presence of both elemental oxygen and hydrogen impurities. The multiscale simulations and subsequent analysis suggest that electronegative surface impurities can inhibit dislocation nucleation from a crack-tip, which is consistent with macroscopic brittle failure. Second, a series of ab-initio and multiscale simulations are performed, directly linking an atomistic mechanism of hydrogen-assisted cracking (HAC) to experimental fatigue data. The mechanism of enhanced surface deformation is demonstrated using an aluminum-only interatomic potential capable of reproducing ab-initio trends by strategically shielding critical surface bonds in accordance with the environmental exposure level. The strategic shielding approach is used within a CADD-based model to predict an embrittling effect of hydrogen on near threshold fatigue crack growth rates. Third, a CADD-based model is used to simulate the approximate effects of monolayer surface layer stiffening

on near-threshold fatigue behavior in aluminum. Stiff surface layer effects are investigated by adding a Lennard-Jones overlay potential to exposed aluminum crack-face atoms. For the single crystal orientation studied, we find that deformation behavior generally begins with a short period of fast transient crack-tip propagation until a stable defect structure has accumulated ahead of the crack. Additionally, the approximate effects of stiff monolayer surface-film formation are found to inhibit crack growth by resisting typical slip-plane cracking behavior. For all studies, the results are discussed in terms of the current environment assisted fatigue literature.

BIOGRAPHICAL SKETCH

Richard Zamora, son of James and Laura Zamora, grew up in the small town of Gladstone, New Jersey. After graduating in the top ten percent of his class at Bernards High School, he attended Cornell University, where he majored in Civil and Environmental Engineering with a concentration on Civil Infrastructure. During his undergraduate study at Cornell, Richard pole-vaulted for the varsity track and field team, achieving both all-ivy-league and NCAA all-east recognitions. He graduated Magna Cum Laude in 2010 with a Bachelor of Science in Civil Engineering, and immediately began his graduate research at Cornell with Professor Derek Warner. In May of 2013 he earned his Masters of Science in Structural Engineering, and then three months later married Yuliana Gomez on a sunny summer afternoon in the Cornell University Plantations. In June of 2014, Richard and Yuliana welcomed their first son into the world, Derek James Zamora. In his spare time, Richard likes to go on outdoor adventures with his family.

To Yuliana, my best friend, my inspiration, and the love of my life. To my son Derek, for changing my life in all the best ways possible. To my family, for providing me with incredible love and support that I would be nowhere without.

ACKNOWLEDGEMENTS

I would first like to thank my advisor, Professor Derek Warner, for encouraging me to pursue a PhD at Cornell. I consider myself lucky to have had the opportunity to work with such an intelligent, upbeat and encouraging mentor. Second, I would also like to thank Professor Christopher Earls for introducing me to the world of computational mechanics research and for providing me with useful advice and support ever since. Third, I would like to thank Professors Anthony Ingraffea and Richard Henning for participating in my graduate committee and for providing me with invaluable feedback and advice throughout my time at Cornell. In addition to those already mentioned, I would also like to acknowledge valuable support from Paul Hess at ONR (Grant No. N000141010323), Ed Glaessgen at NASA (Grant No. NNX08BA39A), Ali Sayir at AFOSR (FA95501110273), the NSF IGERT Fellowship Program (Grant No. DGE-0903653), and the Lester B. Knight Fellowship.

TABLE OF CONTENTS

Biographical Sketch	iii
Dedication	iv
Acknowledgements	v
Table of Contents	vi
List of Tables	viii
List of Figures	ix
1 Introduction	1
2 Ab-initio prediction of environmental embrittlement at a crack tip in aluminum	4
2.1 Abstract	4
2.2 Introduction	4
2.3 QM-CADD Methodology and Setup	7
2.4 QM-CADD Results	8
2.5 Bader Charge Analysis	10
2.6 Continuum Rice-Peierls Model	10
2.7 Discussion	15
2.8 Summary and Conclusions	16
2.9 Acknowledgements	17
3 Illuminating the chemo-mechanics of hydrogen enhanced fatigue crack growth in aluminum alloys	18
3.1 Abstract	18
3.2 Introduction	19
3.3 Hydrogen Binding at an Aluminum Surface	21
3.4 Slip and Decohesion at an Aluminum Surface	23
3.5 Multiscale Fatigue Model: Setup	28
3.5.1 Strategic Bond Shielding Approximation (SBSA)	31
3.6 Multiscale Fatigue Model: Results and Discussion	34
3.7 Conclusion	37
4 Near-threshold fatigue loading in aluminum and the mechanical effects of monolayer surface-layer stiffening	38
4.1 Abstract	38
4.2 Introduction	39
4.3 Background	41
4.4 Methods	42
4.4.1 Multi-scale Framework: Coupled Atomistic and Discrete Dislocations (CADD)	43
4.4.2 Multi-scale Fatigue Model Setup	47
4.5 Results	49

4.5.1	Transient Behavior	50
4.5.2	Irregular Propagation	52
4.5.3	Surface Film Effects	53
4.6	Discussion	55
4.7	Summary and Conclusions	59
5	Conclusion	60
	Bibliography	62

LIST OF TABLES

2.1	Results of the Bader charge transfer analysis, QM-CADD simulations and continuum model simulations. Charge units are displayed as the negative electron charge ($-e$), and K_{IN} units are in $eV/^{2.5}$. The Impurity Effect was calculated as the percent change in K_{IN} with respect to the pure aluminum simulation. The continuum model results assume an effective crack tip radius of $\rho = 2.0$. The continuum predictions confirm the strengthening effects of the QM-CADD simulations, albeit at a smaller magnitude. . . .	14
4.1	Mechanical properties of aluminum supercell with and without a Lennard-Jones overlay potential applied to all atoms. The parameters of the overlay potential were chosen to increase all parameters listed in table 4.1, and to produce an increase in C_{44} roughly comparable to a transition from Al to Al_2O_3 (450-500%). The parameters were also chosen so as to leave the FCC lattice constant effectively unchanged.	45

LIST OF FIGURES

2.1	<p>QM-CADD simulation setup for studying crack tip dislocation nucleation: (a) Overall geometry with color contours showing uniaxial strain in the vertical direction; (b) Zoomed view of the crack tip region, showing the inner ions (grey), the interface ions (black), and the pad ions (white); (c) The Kohn-Sham DFT simulation cell consisting of the inner, interface, and pad ions surrounded by a small vacuum in a periodic unit cell. The 3D atomic structure is projected onto the 2D plane for visual clarity.</p>	7
2.2	<p>Dislocation nucleation process in the presence of environmental impurity atoms: (a) Hydrogen causes nucleation to occur at a stress intensity load of $0.310 \text{ eV}/^{2.5}$. (b) Oxygen causes nucleation to occur at a stress intensity load of $0.300 \text{ eV}/^{2.5}$. Equilibrium crack tip configurations for both impurities are shown at $K_I = 0.235 \text{ eV}/^{2.5}$, where both configurations are stable and dislocation free. In both nucleated configurations, aluminum atoms are shaded by their motion in the slip plane direction relative to the previous load step. It is clear from these images and the fiducial markers that hydrogen causes slip to occur on a different slip plane than oxygen.</p>	9
2.3	<p>Contour images of the valence electron charge density field for each of the three crack tip configurations at $K_I = 0.235 \text{ eV}/^{2.5}$. Atomic positions are projected onto the 2D contour image, which was taken on the plane halfway between atoms in the $[\bar{1}10]$ direction in all three plots: (a) Pure aluminum crack tip configuration, (b) & (c) the same configuration with hydrogen and oxygen added, respectively. Although both impurities have an effect on the charge transfer induced near the slip plane, the resulting charge density fields are clearly different. All contour units are in elementary electron charge (e).</p>	11
2.4	<p>Contour plots for the calculated stacking fault energy surfaces are shown for the pure aluminum, hydrogen and oxygen configurations (from left to right, respectively). The energy vs. slip relationship shows a trend of convergence toward the theoretical bulk stacking fault energy curve with increasing distance from the crack tip. The presence of the free surface clearly raises the stacking fault energy to a depth of 1nm into the material, and both impurity atoms produce an even larger increase in energy within the first few atomic layers.</p>	13

3.1	Typical high cycle fatigue crack growth behavior expected for an Al-alloy over a range of environmental exposure levels. Here, we propose that hydrogen enhanced surface deformation (HESD) must be (at least partially) responsible for the proportional increase in da/dN as a function of P/f between the exposure (T_{Exp}) and saturation (T_{Sat}) thresholds (the highlighted area). Detailed descriptions of exposure regimes (i)-(iii) are presented in the text. The inset shows an HESD susceptible crack-tip system. Here, the crack-tip is not yet saturated by oxide formation, and an atomized hydrogen concentration is present on the surface. Large (dark-grey) atoms are aluminum, medium (red) atoms are oxygen and small (light-grey) atoms are hydrogen.	20
3.2	Binding energies (E_B^H) for a variety of isolated interstitial hydrogen impurity sites at a $\{111\}$ aluminum surface, according to equation 3.1. All calculations were performed using the PAW-PBE Al and H pseudopotentials in VASP [23].	23
3.3	(a) The periodic simulation cell used to calculate $E_{DFT}^{Surf+H}(\Delta_a)$. The B cell vector (not shown) is perpendicular to the A-C plane, and pointing into the page. Note that both the A-B and B-C cell boundaries are in the $\{111\}$ family of planes. The grey atoms represent the next periodic image of the simulation cell in the C direction. (b) Summary of $\Gamma'_{decohesion}$ plotted on the imposed decohesion plane. Results are colored according to the %-change in $\Gamma'_{decohesion}$ relative to the hydrogen-free calculation for the same $\{111\}$ surface.	26
3.4	Plots of Γ'_{slip} for an aluminum surface with and without hydrogen. (a) and (b) show Γ'_{slip} for hydrogen in the fcc and first tetrahedral-B sites for ACUTE step formation, respectively. (c) and (d) depict Γ'_{slip} for hydrogen in the fcc and first tetrahedral-B sites for OBTUSE step formation, respectively. In each plot, the hydrogen-free calculation is plotted as a dashed line for reference, and the hydrogen binding site of interest was considered on three different atomic planes lying parallel to the A-B cell boundary. Plane 1 is on the A-B cell boundary, Plane 2 is on the next plane above the cell boundary and Plane 3 is on the next plane below the cell boundary.	27

3.5	(a)-(b) CADD simulation setup, as discussed in the text and references [2, 47]. (a) Geometry of the continuum discrete dislocation domain, where boundary conditions are applied. (b) A simple embedded atomistic domain is shown for illustrative purposes. Behavior of grey and black atoms is defined by SBSA enhanced EAM molecular mechanics. Behavior of white atoms is interpolated from the elastic continuum displacements. (c)-(d) Typical crack-tip deformation mechanisms varied at low to moderately high growth rates. Here, we see that the same moderately high crack growth rate ($\sim 10/\text{cycle}$) can be a result of both slip band cracking and brittle cleavage. In (c), red dashed lines are used to highlight active slip planes.	29
3.6	Comparison of CADD simulation results with experimental fatigue data for a C433 aluminum alloy. Units for crack growth rate, da/dN , are $/\text{cycle}$. For simulation data points (shown in green), environmental exposure is in units of average number of allowed shielding events per load cycle. For experimental data points (shown as black circles, obtained from reference [44]), environmental exposure is in units of $Pa \cdot s$. The horizontal green and black dashed arrows show the approximate growth rates in vacuum for simulation and experiment, respectively.	34
4.1	Illustration of the CADD multiscale methodology, as discussed in the text and references [2, 47, 8, 48]. The left-hand image shows the geometry of the continuum discrete dislocation domain, where boundary conditions are applied. The right-hand image shows an atomistic domain, which has been miniaturized for illustrative purposes. For the simulations presented in this work, the behavior of grey and black atoms are defined by embedded atom model (EAM) molecular mechanics. Behavior of white atoms is interpolated from the elastic continuum displacements.	42
4.2	An illustration of the volume grid used to track crack-tip propagation and detect surface atoms for adding an overlay potential. Free-space volume grid cells are shaded in gray, while solid cells are white. Surface atoms experiencing overlay potential effects are showed in yellow, while all other atoms are shown in red. . .	46

4.3	A snapshot of the actual atomistic domain and surrounding continuum mesh. The region highlighted in red is the mesh corresponding to the free and interface atoms modeled by EAM molecular mechanics (pad atom nodes are not shown to be overlapping with the courser continuum domain). The region highlighted in yellow shows the area along the continuum crack surfaces where the crack-tip opening distance is calculated at a constant distance from the current crack-tip location. Finally, the yellow line drawn over the red atomistic region shows the band of atoms where dislocations are detected and passed to the continuum domain. The details of dislocation passing are discussed in references [2, 47].	48
4.4	The first major deformation event experienced in the majority of simulations is dislocation nucleation from the primary slip plane intersecting the crack front. (a) Shows the nucleation of a dislocation along the primary slip plane (labeled with a dashed line). (b) Continued dislocation nucleation of the primary slip plane leads to a localized disordering of atoms to accommodate shear-tension coupling along the surface. To highlight the defect structures, atoms with non-FCC coordination are colored, while FCC atoms are grey.	50
4.5	An in-vacuo fatigue simulation shown after 15 fatigue cycles. Red lines are used to label planes on which a full dislocation has nucleated and glided away from the surface. To highlight the defect structures, atoms with non-FCC coordination are colored, while FCC atoms are grey. It is clear that the majority of dislocation nucleation occurs during the early stages of deformation when crack growth is the fastest.	52
4.6	Curves depict the average location of the crack-tip for each fatigue load-range considered as a function of the current load cycle number. Loads listed in legend have units of $meV/\text{\AA}^{2.5}$. In legend, V denotes in-vacuo results, while ML denotes monolayer surface stiffening results.	54
4.7	During the early stages of crack-tip deformation and propagation, stiff surface film formation clearly inhibits the nucleation of dislocations along the primary slip plane. (a) & (b) Show crack-tips with stiff monolayer surface film coverage after two full load cycles. (c) Shows an in-vacuo crack-tip after the same loading has been performed.	55

4.8	Although the average crack-growth distances observed within the first five loading cycles range from about 1-6 Å/cycle depending on the specific load range and presence of a surface film, the crack-growth rates slow dramatically as the loading progresses. Nevertheless, the approximate growth rates determined from a linear fit predict increased $\frac{da}{dN}$ in a vacuum environment. Error bars depict half the standard deviation distance in each direction.	56
4.9	Plot of the average crack-tip position as a function of fatigue load cycle. Here, 32 load cycles were considered at $\Delta K = 0.275 \text{ eV}/\text{Å}^{2.5}$ for both in-vacuo and surface-film conditions. Error bars depict half the standard deviation distance in each direction.	57

CHAPTER 1

INTRODUCTION

Despite decades of research on the phenomenon of fatigue crack growth in structural metals, the specific atomistic mechanisms governing near-threshold crack-tip propagation remain unclear [43, 37, 55, 38]. Due to the length and time-scale limitations of current experimental capabilities, the most promising path to a comprehensive understanding of near-threshold fatigue is likely through direct, physics-based, atomistic simulation. Unfortunately, many significant challenges tend to prevent researchers from producing atomistic models capable of capturing true fatigue mechanisms in real alloys [12, 13, 17].

Among the most daunting of these challenges, is the incorporation of realistic environmental effects. Typically, atomistic simulations are limited by the approximation of an inert chemical environment [12, 13, 58, 17, 61]. Unfortunately, it is well known that the characteristics of aluminum fatigue change dramatically when observed in a vacuum environment rather than ambient air [52, 5]. Furthermore, the failure rates tend to increase with the level of environmental humidity [44, 45, 59]. Accordingly, the purpose of the three papers composing this dissertation is to illuminate the poorly understood atomistic-scale mechanisms governing environmentally assisted fatigue.

The second chapter, entitled “Ab-initio prediction of environmental embrittlement at a crack tip in aluminum,” is published as a *Rapid Communication* in Physical Review B, and was selected as an *Editors Suggestion*. Co-authors include Prof. Arun Nair, Prof. Richard Hennig and Prof. Derek Warner. This work details the use of an ab-initio atomistic-continuum multiscale framework to simulate the behavior of a loaded crack tip in the presence of oxygen and hy-

drogen. The multiscale simulations and subsequent analysis suggest that electronegative surface impurities can inhibit dislocation nucleation from a crack-tip, which is consistent with macroscopic brittle failure. The highlight of the analysis is the formulation and implementation of Pierels model used to predict the effects of surface binding on the critical load required for dislocation nucleation.

The third chapter, entitled “Illuminating the chemo-mechanics of hydrogen enhanced fatigue crack growth in aluminum alloys,” was co-authored by Dr. Kristopher Baker and Prof. Derek Warner. This work uses a series of computational studies, across multiple length scales, to directly link an atomistic mechanism of hydrogen assisted cracking to experimental fatigue data. The study begins with an ab-initio investigation of the effects of hydrogen bonding on slip and decohesion at a $\{111\}$ aluminum surface. An aluminum-only interatomic potential is then modified to reproduce ab-initio trends by strategically shielding critical surface bonds in accordance with the environmental exposure level. Finally, the strategic shielding approach is used within a coupled atomistic-continuum discrete dislocation framework to predict the effect of hydrogen on near threshold fatigue crack growth rates.

The fourth chapter, entitled “Near-threshold fatigue loading in aluminum and the mechanical effects of monolayer surface-layer stiffening,” was co-authored by Prof. Derek Warner. This work details the use of a concurrently coupled atomistic and discrete dislocation multiscale method (CADD) to directly simulate crack-tip deformation and propagation during near-threshold fatigue loading in aluminum. The effects of environmental monolayer surface-film stiffening are investigated by adding a Lennard-Jones overlay potential to

exposed aluminum crack-face atoms. The effects of surface layer stiffening are found to clearly inhibit crack growth, and several resulting insights are highlighted.

CHAPTER 2

AB-INITIO PREDICTION OF ENVIRONMENTAL EMBRITTLEMENT AT A CRACK TIP IN ALUMINUM

2.1 Abstract

This letter reports on ab-initio predictions of environmental embrittlement in aluminum. We have used an atomistic-continuum multiscale framework to simulate the behavior of a loaded crack tip in the presence of oxygen and hydrogen. The multiscale simulations and subsequent analysis suggest that electronegative surface impurities can inhibit dislocation nucleation from a crack tip, which is consistent with macroscopic brittle failure. The metal-impurity bonding characteristics have been analyzed using a Bader charge transfer approximation, and the effect of this bond on the theoretical slip distribution has been investigated using a continuum Pierels model. The Pierels model, which is a function of the position dependent stacking fault energy along the slip plane, was used to estimate the effects of several common environmental impurities.

2.2 Introduction

Aluminum alloys are extremely popular structural materials in today's engineering world. This popularity is well deserved, as aluminum alloys have a remarkably low density relative to their stiffness and strength. Aluminum alloys are also naturally resistant to corrosion due to their natural formation of passivating oxide thin-films in oxygen environments. Although this hard film

formation generally protects aluminum from mechanical wear and corrosion, the brittle oxide material is also highly susceptible to rupture in areas of high stress concentration, i.e. at a loaded crack-tip. For this reason, aluminum alloys are not immune to environment assisted crack growth. This is especially true in the case of near-threshold fatigue loading, when the protective oxide film is frequently (or even continuously) ruptured at the slowly propagating crack-tip.

The presence of environmental impurities is known to promote crack growth in a variety of technologically important materials [15]. For example, when aluminum is subjected to cyclical loading in a controlled atmosphere, a rise in humidity will accelerate the crack growth process and lower the threshold load required for fatigue to occur [52]. To explain the origin of this environmental embrittlement phenomenon, a wide variety of theoretical mechanisms have been hypothesized from a top-down approach, using the wealth of experimental data and microscopy presented in the literature [29, 26].

It is now possible to use atomistic modeling capabilities to investigate classical embrittlement mechanisms from a bottom-up approach [51, 19, 1, 27]. Such models can be used to observe bond rupture as it occurs, thus potentially illuminating new chemo-mechanical details that have yet to be proposed. In the past, atomistic modeling was limited when used to investigate fracture processes, because it was a significant challenge to enforce accurate interatomic force calculations while considering long range elastic interactions. Fortunately, growing supercomputing resources and advances in concurrent multiscale modeling techniques [4, 46, 35, 33] are now beginning to make accurate atomic-scale simulations of crack growth more feasible.

In this spirit, the current work provides the first direct ab-initio glimpse into

the chemo-mechanical interactions that occur at a metal crack tip in the presence of environmental surface impurities. The crack tip simulations were made possible by combining the newly developed quantum mechanical coupled atomistic discrete dislocation (QM-CADD) framework and the NASA Pleiades supercomputer.

We have examined three distinct crack tip configurations: (1) a crack tip with no impurities, (2) a crack tip with a single hydrogen impurity, and (3) a crack tip with a single oxygen impurity. Each simulation was initialized at a stable stress intensity factor and the load was ramped through a succession of increments until equilibrium could no longer be reached without the nucleation of a partial dislocation. To estimate the relative charge transfer induced by each impurity, a Bader analysis was performed on the electron charge density solution for each configuration at the same load. The mechanical effect of the perturbed charge distribution was determined by calculating the energetic resistance to shear along each slip plane. This energy functional was used within a continuum Peirls model to arrive at a critical load prediction. A consistent strengthening effect was observed for all crack tip simulations in the presence of oxygen and hydrogen. Although the continuum model yields a similar strengthening effect for any electro-negative surface impurity, the results of QM-CADD suggest that a unique embrittlement mechanism takes place in the presence of hydrogen.

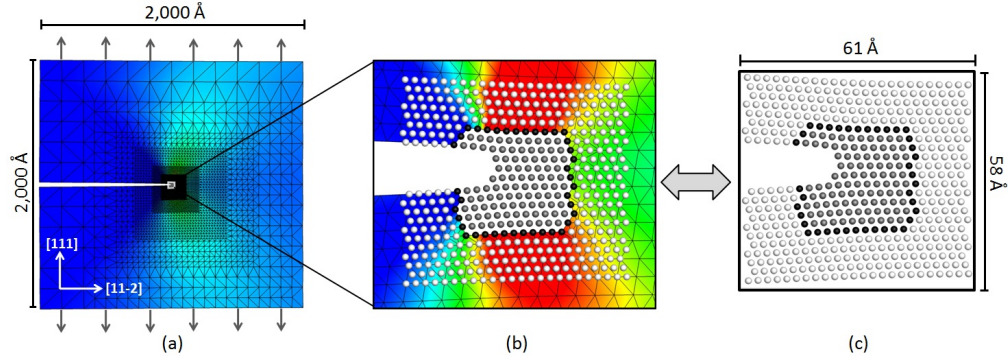


Figure 2.1: QM-CADD simulation setup for studying crack tip dislocation nucleation: (a) Overall geometry with color contours showing uniaxial strain in the vertical direction; (b) Zoomed view of the crack tip region, showing the inner ions (grey), the interface ions (black), and the pad ions (white); (c) The Kohn-Sham DFT simulation cell consisting of the inner, interface, and pad ions surrounded by a small vacuum in a periodic unit cell. The 3D atomic structure is projected onto the 2D plane for visual clarity.

2.3 QM-CADD Methodology and Setup

The QM-CADD atomistic-continuum framework is a reliable way to investigate crack tip mechanisms involving complex metal-impurity bonding. The multi-scale framework allows for the computation of high fidelity interatomic forces by requiring that only the small nonlinear region of material surrounding the crack tip is modeled atomistically. Here we use Kohn-Sham Density Functional Theory (KS-DFT) in the atomistic region and linear elastic finite elements in the surrounding region (see figure 2.1). The two regions are coupled by an iterative force balance approach, and the relevant coupling errors have been minimized by the methods discussed in [34, 33]. Broadly, one can consider the QM-CADD approach to be identical to its ancestor, developed by Shilkrot *et al.* [47], but with the original empirical potential driven inter-atomic force calculation replaced by a quantum-mechanical Hellman-Feynman force calculation [23].

All simulations were built upon the ductile aluminum crack tip geometry depicted in figure 2.1. In this configuration, we use a $20,000 \times 20,000$ continuum domain with a crack, terminating at a 58×55 atomistic region. The crack was created by removing three (111) planes from a pristine material, preventing the crack from closing at small loads. The resulting atomistic region consisted of a total of 442 aluminum atoms, of which 326 were distributed in the pad region in order to buffer the crack tip from possible vacuum effects.

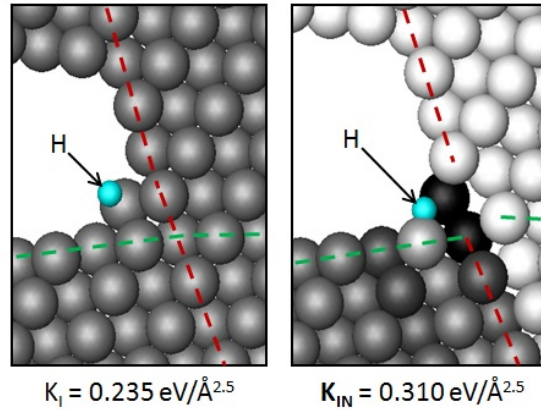
All interatomic force calculations were performed within the Vienna Ab-initio Simulation Package (VASP), in which ultra-soft pseudopotentials and a plane wave basis set were used to solve the equations of (KS-DFT) [24]. Within VASP, the local density approximation (LDA) was used, along with a $1 \times 1 \times 8$ k-point mesh, a Methfessel-Paxton smearing of 1 eV [30] and a plane wave cutoff of 250 eV. All atomistic visualization was performed in VESTA [31].

A meaningful atomistic discretization of the continuous charge density field was obtained by dividing space into regions using a Bader surface designed to satisfy the relationship: $\nabla\rho(\vec{r}_s) \cdot \hat{n}(\vec{r}_s) = 0$, where \vec{r}_s is a point on the Bader surface and $\hat{n}(\vec{r}_s)$ is the normal vector to the surface at that point.

2.4 QM-CADD Results

Using the QM-CADD framework to model the pure aluminum crack tip configuration, the critical load required for nucleation was found to occur at a stress intensity of $0.245 \text{ eV}/^{2.5}$. At this load there was a clear relative motion of atoms across the $(11\bar{1})$ plane in the $[112]$ direction, indicative of the nucleation of a partial dislocation from the free surface. As expected for a ductile metal, plasticity

(a) Nucleation near hydrogen impurity



(b) Nucleation near oxygen impurity

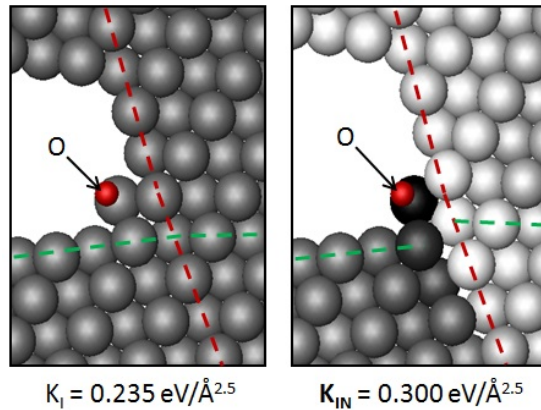


Figure 2.2: Dislocation nucleation process in the presence of environmental impurity atoms: (a) Hydrogen causes nucleation to occur at a stress intensity load of $0.310 \text{ eV}/\text{\AA}^{2.5}$. (b) Oxygen causes nucleation to occur at a stress intensity load of $0.300 \text{ eV}/\text{\AA}^{2.5}$. Equilibrium crack tip configurations for both impurities are shown at $K_I = 0.235 \text{ eV}/\text{\AA}^{2.5}$, where both configurations are stable and dislocation free. In both nucleated configurations, aluminum atoms are shaded by their motion in the slip plane direction relative to the previous load step. It is clear from these images and the fiducial markers that hydrogen causes slip to occur on a different slip plane than oxygen.

occurred on the most highly sheared slip plane without any sign of incipient cleavage or crack advancement.

The presence of oxygen and hydrogen at the surface of the crack tip was

observed to increase the critical nucleation load. While oxygen resulted in dislocation nucleation on the same slip plane as in the pure aluminum case, hydrogen resulted in dislocation nucleation on a different slip plane (figure 2.2). More specifically, the presence of hydrogen led to crack advancement by a single atomic spacing and dislocation nucleation on the newly exposed slip plane. Thus, both impurity elements were observed to inhibit crack tip plasticity, while hydrogen qualitatively changed the response of the crack tip in that it led to incremental crack advancement.

2.5 Bader Charge Analysis

Figure 2.3 shows the KS-DFT electron charge density solutions calculated during QM-CADD simulations at a stable load of $K_I = 0.235 \text{ eV}/^{2.5}$. The results of the Bader analysis [57] of the valence charge density in Table 2.1 show that oxygen and hydrogen both form an ionic bond with the nearest aluminum atom, leading to a filled valence shell, as expected from electronegativity differences. The charge transfer at the impurity site clearly influences the interatomic bonding across the slip plane, which is ultimately the source of the higher critical nucleation loads observed in the mechanical simulations.

2.6 Continuum Rice-Peierls Model

To better understand this process, we analyzed the crack tip dislocation nucleation mechanism using an atomistically informed Peierls continuum model [41]. The Peierls model simplifies the dislocation nucleation process to a continuum

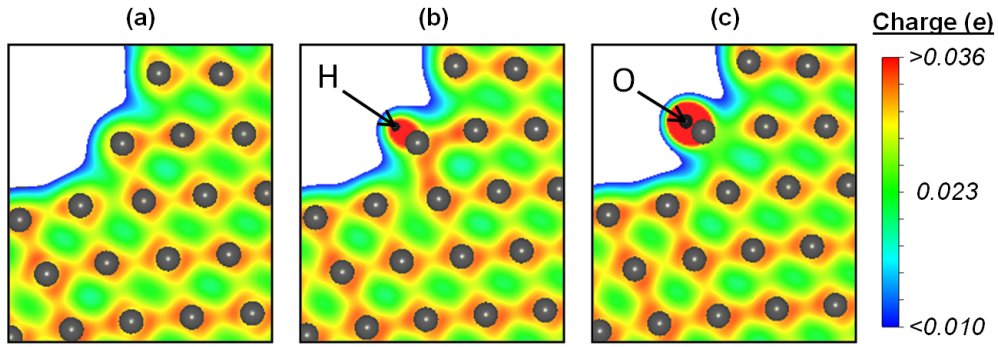


Figure 2.3: Contour images of the valence electron charge density field for each of the three crack tip configurations at $K_I = 0.235 \text{ eV}/^{2.5}$. Atomic positions are projected onto the 2D contour image, which was taken on the plane halfway between atoms in the $[\bar{1}10]$ direction in all three plots: (a) Pure aluminum crack tip configuration, (b) & (c) the same configuration with hydrogen and oxygen added, respectively. Although both impurities have an effect on the charge transfer induced near the slip plane, the resulting charge density fields are clearly different. All contour units are in elementary electron charge (e).

mechanics problem involving a loaded linear elastic body with an embedded slip plane capable of producing a shear displacement jump in the material. Accordingly the energy of the model system is then a function of the elastic strain energy stored in the bulk material and the nonlinear localized energy penalty associated with slip on the slip plane, *i.e.* the stacking fault energy curve. At low loads, a unique slip distribution exists that corresponds to the unstable equilibrium state of the system (the barrier state for dislocation nucleation). The minimum load at which this barrier state ceases to exist represents the critical load for dislocation nucleation to occur instantaneously.

Traditionally, the stacking fault energy curve is often assumed to be independent of position [41, 58, 56]. This effectively corresponds to ignoring the influence of the free surface on interatomic bonding. Alternatively, in this analysis we computed the stacking fault energy curve using KS-DFT as a function of

both plastic slip and distance along the slip plane from the crack surface, r . This was accomplished by rigidly shearing the crack tip configuration used in the QM-CADD simulation along the slip plane and integrating Hellman-Feynman forces to define the stacking fault energy curve as a function of r .

The energy balance relationship used in the continuum Peierls dislocation model is

$$U[\delta(r)] = U_o + \int_0^{\infty} \Phi[\delta(r), r] dr + \frac{1}{2} \int_0^{\infty} s[\delta(r)] \delta(r) dr - \int_0^{\infty} \sigma_{r\theta}(r) \delta(r) dr. \quad (2.1)$$

In this relationship U_o is the energy of the loaded elastic system in which the slip distribution, $\delta(r)$, is confined to be zero along the slip plane. $\Phi[\delta(r), r]$ is the local nonlinear component of the energy penalty associated with slip and is derived from the stacking fault energy curves [41], e.g. figure 2.4. $s[\delta(r)]$ is the stress distribution on the slip plane created by the slip distribution,

$$s[\delta(r)] = \frac{\mu}{2\pi(1-\nu)} \int_0^{\infty} \sqrt{\frac{\xi}{r}} \frac{d\delta(\xi)/d\xi}{r-\xi} d\xi. \quad (2.2)$$

The remaining term in equation (2.1) represents the elastic work done by the slip distribution acting against the applied load, $\sigma_{r\theta}(r, \rho, K_I, \theta)$. The relevant form of the applied load, as derived in Ref. [7], is dependent upon the radius of curvature of the crack tip, ρ , the applied stress intensity factor, K_I , and the orientation of the slip plane, θ . In the calculations conducted here, the shear modulus (μ) was taken as 46.9 GPa and the crack tip radius as 2.0 . The critical nucleation load was obtained by incrementing the applied stress intensity factor until the slip distribution corresponding to the local minimum of equation 2.1 failed to converge. For each load increment the equilibrium slip distribution was found numerically using a standard Newton-Raphson approach.

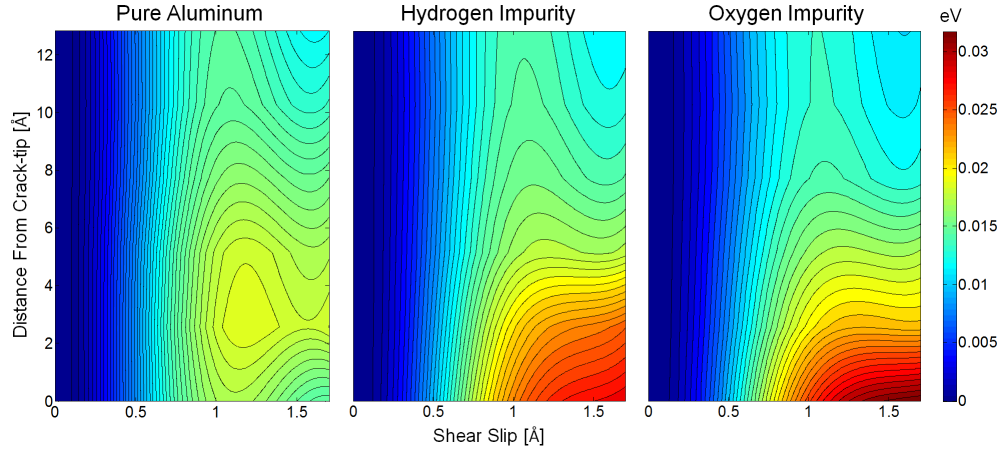


Figure 2.4: Contour plots for the calculated stacking fault energy surfaces are shown for the pure aluminum, hydrogen and oxygen configurations (from left to right, respectively). The energy vs. slip relationship shows a trend of convergence toward the theoretical bulk stacking fault energy curve with increasing distance from the crack tip. The presence of the free surface clearly raises the stacking fault energy to a depth of 1nm into the material, and both impurity atoms produce an even larger increase in energy within the first few atomic layers.

The stacking fault energies were found to be significantly influenced by the free surface to a depth of 1 nm into the material, beyond this scale the energies approached that of the bulk. The influence of surface impurities on the stacking fault energy was found to have a similar range (figure 2.4). Considering that the critical state for partial dislocation nucleation from an aluminum crack tip involves a dislocation very close the surface (~ 1 nm) [58], substantial inaccuracies can result if the bulk stacking fault energies are used in the model. This finding justifies the approach taken here.

Despite its simplifying assumptions the Peierls continuum model predicts that both hydrogen and oxygen inhibit crack tip plasticity in agreement with the QM-CADD simulations (Table 2.1). Given the continuum model's success at reproducing the QM-CADD simulation results, it was used to examine the

Impurity Type	Bader Charge		QM-CADD		Continuum	
	Impurity	Nearest Al	K_{IN}	Impurity Effect	K_{IN}	Impurity Effect
Pure Al	-	-0.02	0.245	-	0.246	-
Hydrogen	-1.27	1.36	0.310	27%	0.265	7.8%
Oxygen	-2.11	2.26	0.300	22%	0.265	7.8%
Chlorine	-1.20	1.07	-	-	0.258	5.0%
Flourine	-1.23	1.20	-	-	0.259	5.4%
Sodium	1.00	-0.42	-	-	0.248	0.8%
Lithium	1.00	-0.87	-	-	0.245	-0.4%

Table 2.1: Results of the Bader charge transfer analysis, QM-CADD simulations and continuum model simulations. Charge units are displayed as the negative electron charge ($-e$), and K_{IN} units are in $eV/^{2.5}$. The Impurity Effect was calculated as the percent change in K_{IN} with respect to the pure aluminum simulation. The continuum model results assume an effective crack tip radius of $\rho = 2.0$. The continuum predictions confirm the strengthening effects of the QM-CADD simulations, albeit at a smaller magnitude.

effect of four additional impurity elements. Considering that chlorine, fluorine, lithium and sodium relax to a similar location at the crack tip, the prediction of their impact on nucleation was amenable to the continuum model. While fluorine and chlorine both exhibited a strengthening effect, neither impurity is predicted to have as strong of an effect as oxygen and hydrogen. In contrast, sodium and lithium each had a negligible effect on the critical nucleation load, both creating less than a 1% change in the critical load relative to pure aluminum. Loosely speaking, these results are consistent with the general understanding that surface impurities affect the bond strength on the slip plane through localized charge transfer. While the addition of electropositive atoms like lithium and sodium produced negligible perturbations in the charge density field of the crack tip, the other electronegative impurities had a much larger effect.

2.7 Discussion

In the literature, environmental embrittlement at the crack tip is often attributed to impurities weakening interatomic bonding, and therefore enhancing decohesion [32, 36, 19] and/or crack tip dislocation emission [28]. At first sight, the ab-initio predictions made here are in direct contrast to the idea that impurity elements such as hydrogen enhance dislocation emission at the crack tip. However, further consideration is warranted, in that it is possible that the presence of impurities may force dislocations to be nucleated on the slip plane immediately in front of the crack tip, as observed here in the case of hydrogen (figure 2.2). This would ultimately inhibit crack tip blunting, which requires dislocation nucleation on multiple slip planes, leading to a more brittle macroscopic response.

The idea that the presence of impurities at the crack tip lowers the cohesive energy is another mechanism that may lead to embrittlement. This mechanism is consistent with ab-initio predictions that show that the presence of hydrogen on a potential crack plane in bulk aluminum lowers the cohesive energy of that plane [19]. Here we examined the role of surface hydrogen on the cohesive energy of the crack plane which was activated in the QM-CADD simulation with hydrogen. For the configuration examined here, the cohesive energy was not found to be influenced by the presence of hydrogen on the surface of the crack. Thus, the crack tip hydrogen embrittlement observed in our QM-CADD simulation can solely be attributed to hydrogen inhibiting dislocation nucleation.

Overall, it is important to recognize that the findings of this work are likely sensitive to the specific atomic configuration of the crack tip and impurity ele-

ments that were studied, noting that the impurity elements were placed in the surface location where we suspect they would most strongly influence dislocation nucleation. Further, the surface oxide layer, a key feature in real-world problems, has not been considered.

2.8 Summary and Conclusions

In summary, we have performed three direct quantum mechanical multiscale simulations of a loaded crack tip, predicting that hydrogen and oxygen surface impurities inhibit the onset of plasticity. While the addition of oxygen allowed the onset of plasticity to occur on the same slip plane as the pure aluminum configuration, the addition of hydrogen forced plasticity to occur on an alternate slip plane, leading to incremental crack growth. In order to obtain more insight into the inhibition of plasticity by surface impurity elements, we have employed a quantum mechanically informed continuum model to predict the critical load at which a dislocation will nucleate from the crack tip. The continuum model confirmed the impurity strengthening mechanism found in the multiscale model, thus more firmly establishing that plasticity can be inhibited by surface impurities. When compared to other work with bulk impurities, it is clear that the strengthening mechanism observed here is dependent on the geometry of the surface and the depth of adsorption. These factors motivate a new understanding of embrittlement mechanisms.

2.9 Acknowledgements

This primary support for this research was provided by Paul Hess at ONR (Grant No. N000141010323). Additional support was provided by Ed Glaessen at NASA (Grant No. NNX08BA39A), Ali Sayir at AFOSR (FA95501110273), and the NSF IGERT Program (Grant No. DGE-0903653).

CHAPTER 3
ILLUMINATING THE CHEMO-MECHANICS OF HYDROGEN
ENHANCED FATIGUE CRACK GROWTH IN ALUMINUM ALLOYS

3.1 Abstract

The presence of elemental hydrogen is known to accelerate fatigue crack growth in aluminum alloys. However, a direct link between experimental data and the governing atomistic mechanisms has remained elusive. Here we present a series of computational studies, across multiple length scales, directly linking an atomistic mechanism to experimental data for a specific aluminum alloy. Starting with an *ab initio* investigation of hydrogen bonding near a $\{111\}$ aluminum surface, we quantify the effects of hydrogen surface impurities on slip and decohesion. We then modify an aluminum-only interatomic potential to reproduce *ab initio* trends by strategically shielding critical surface bonds in accordance with the environmental exposure level. The strategic shielding approach is used within a coupled atomistic-continuum discrete dislocation framework to predict the effect of hydrogen on near threshold fatigue crack growth rates. The predicted trends agree with published experimental data, suggesting that hydrogen enhanced surface deformation is a key failure mechanism for aluminum alloys in humid environments.

3.2 Introduction

When an aluminum alloy is cyclically loaded (fatigued) at low loads in a controlled environment, an increase in humidity will significantly decrease the time to failure [52, 44, 59]. This is especially true when an edge crack is present on the surface of the loaded material. In this case, the exposed metallic surface at the advancing crack-tip is free to react with water and oxygen molecules in the air, a reaction which generates atomized hydrogen impurities in addition to an oxide film [14]. The presence of atomized hydrogen is experimentally linked to enhanced crack growth rates, a process commonly referred to as hydrogen assisted cracking (HAC) [59].

During a typical high cycle fatigue test, the relationship between the crack growth rate (da/dN) and the environmental exposure level (P/f) follows the general trend illustrated in figure 3.1. The exposure level, defined as the atmospheric pressure of water vapor (P) divided by the loading frequency (f), approximately describes the amount of water vapor available to react with the aluminum surface at the crack-tip per loading cycle. As stated, the H_2O -Al interaction is known to produce atomized hydrogen impurities, making P/f also proportional to the crack-tip hydrogen concentration. Depending on the value of P/f , the crack growth behavior can be classified into one of three general regimes: (i) Below the exposure threshold (T_{Exp}), the growth rate will be unaffected by exposure. (ii) Between T_{Exp} and the saturation threshold (T_{Sat}), the growth rate will increase proportionally with exposure. (iii) Above T_{Sat} , the growth rate will either plateau or continue to increase at a lower rate before reaching a plateau [44, 59].

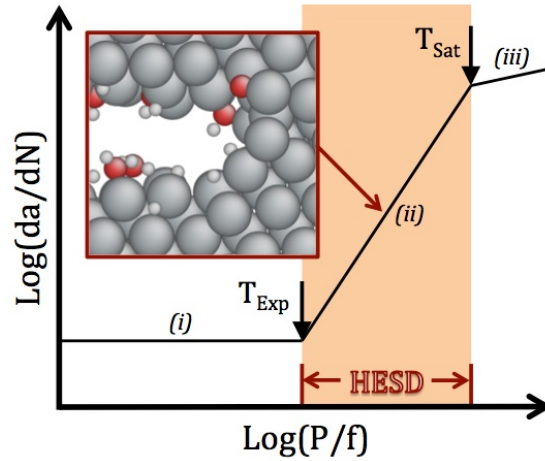


Figure 3.1: Typical high cycle fatigue crack growth behavior expected for an Al-alloy over a range of environmental exposure levels. Here, we propose that hydrogen enhanced surface deformation (HESD) must be (at least partially) responsible for the proportional increase in da/dN as a function of P/f between the exposure (T_{Exp}) and saturation (T_{Sat}) thresholds (the highlighted area). Detailed descriptions of exposure regimes (i)-(iii) are presented in the text. The inset shows an HESD susceptible crack-tip system. Here, the crack-tip is not yet saturated by oxide formation, and an atomized hydrogen concentration is present on the surface. Large (dark-grey) atoms are aluminum, medium (red) atoms are oxygen and small (light-grey) atoms are hydrogen.

Here, we will focus on regime (ii), where da/dN is expected to increase proportionally with the environmental exposure level. In this regime, we can assume that the crack-tip will never become saturated by oxide formation [44, 59], allowing for a range of possible surface coverages below the level of passivation. In the simulations discussed here, we consider only aluminum-hydrogen interactions, and leave the chemo-mechanical effects of oxide coverage for future study.

While HAC is often used to describe accelerated crack growth at exposure levels above T_{Exp} , the exact chemo-mechanical origins are rarely agreed upon. In

the literature, HAC is often assumed to occur by mechanisms like Hydrogen Enhanced Decohesion (HEDE) [36, 32, 19], in which impurities reduce surface energies and encourage decohesion, or by Adsorption Induced Dislocation Emission (AIDE) [28] and Hydrogen Enhanced Localized Plasticity (HELP) [3, 50], in which impurities encourage dislocation emission and mobility. Although each of these mechanisms has been supported by one or both theoretical and experimental studies [19, 53, 50, 45], none has been explicitly used to predict experimental data within a physics based model.

Here, we have used electronic structure calculations to confirm that atomic hydrogen will accelerate both cleavage and dislocation slip at an exposed aluminum surface, a process that we will refer to as hydrogen enhanced surface deformation (HESD). Following this hypothesis, we used direct atomistic simulations to demonstrate that the HESD process accelerates the rate of fatigue crack growth in a manner consistent with experimental results. The atomistic simulations were performed using a concurrently coupled atomistic-discrete dislocation multiscale modeling framework, the bond shielding approximation developed here, and a well established empirical potential for pure aluminum.

3.3 Hydrogen Binding at an Aluminum Surface

To quantify the effects of near surface hydrogen impurities on slip and decohesion, we started by examining the near surface binding energy landscape to identify the most probable atomic sites for hydrogen to reside. Considering the fact that a crack-tip is essentially a free surface, we approximated the binding energy landscape of atomized hydrogen impurities at an aluminum crack-tip by

considering a variety of interstitial sites near a simple $\{111\}$ surface. Using the Kohn-Sham Density functional Theory (KS-DFT) approach [22], we determined a range of possible binding energies (E_B^H) by equation 3.1. Where, E_{DFT}^H is the energy of an isolated hydrogen atom, E_{DFT}^{Al} is the energy of a pure $\{111\}$ surface and E_{DFT}^{H+Al} is the energy of a $\{111\}$ surface with an adsorbed hydrogen atom. A summary of the binding energy results is given in figure 3.2.

$$E_B^H = [E_{DFT}^{H+Al} - (E_{DFT}^{Al} + E_{DFT}^H)]. \quad (3.1)$$

All KS-DFT calculations were performed within the Vienna ab-initio Simulation Package (VASP) [23], utilizing PAW pseudopotentials in conjunction with the PBE exchange-correlation approximation at a plane wave energy cutoff of 450 eV. All k-point meshes were scaled to match a 15x15x15 Monkhorst-Pack grid for a primitive fcc unit cell. Only one k-point was used in directions with vacuum. Equilibrium geometries were obtained by relaxing atoms to a force tolerance of 20 meV.

Overall, the binding energy predictions agree with other ab initio work [60, 53], supporting the popular wisdom that an isolated hydrogen impurity will most likely occupy a surface position in the absence of unsaturated sub-surface vacancies and dislocation cores. Furthermore, considerations of biaxial and uniaxial strain were not found to significantly change the favorability of the free surface over sub-surface sites. Therefore, the energetic favorability of hydrogen ingress does not seem to depend strongly on the elastic stress state near the surface.

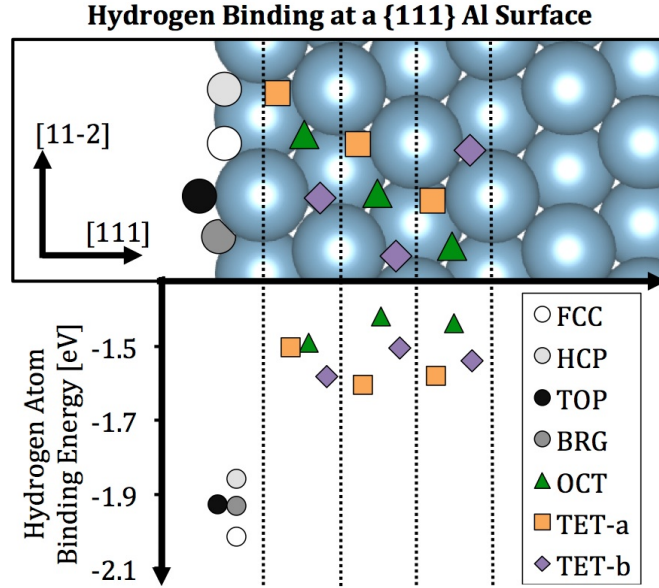


Figure 3.2: Binding energies (E_B^H) for a variety of isolated interstitial hydrogen impurity sites at a $\{111\}$ aluminum surface, according to equation 3.1. All calculations were performed using the PAW-PBE Al and H pseudopotentials in VASP [23].

3.4 Slip and Decohesion at an Aluminum Surface

Having investigated the binding energy landscape of an isolated hydrogen impurity near a simple $\{111\}$ aluminum surface, we subsequently examined hydrogens effect on the energetics of decohesion and slip for the most probable sites presented in figure 3.2. More specifically, we used KS-DFT to investigate the effect of a hydrogen impurity on the energy change in the first three atomic layers at a $\{111\}$ surface during an applied displacement. The choice to study the first three atomic surface layers was motivated by two considerations: (1) the importance of these layers in the cleavage and dislocation emission processes, and (2) the very local effect that a free surface and hydrogen impurity have on aluminum bonding [63].

The energy change, Γ'_a , per unit thickness, t , of the first three surface layers was calculated for two cases of applied displacement, Δ_a , acting either normal, $a = \text{decohesion}$, or parallel, $a = \text{slip}$, to a $\{111\}$ plane. Thus, we define

$$\Gamma'_a(\Delta_a) = E_a^{Surf+H}(\Delta_a) + \frac{\Gamma_a(\Delta_a)A^{3Layers}}{t}, \quad (3.2)$$

where

$$\Gamma_a(\Delta_a) = \frac{E_{DFT}^{Bulk}(\Delta_a) - E_{DFT}^{Bulk}(0)}{A_{DFT}^{Bulk}n}, \quad (3.3)$$

and

$$E_a^{Surf+H}(\Delta_a) = \frac{1}{2t} \left(\frac{E_{DFT}^{Surf+H}(\Delta_a) - E_{DFT}^{Surf+H}(0)}{n} - \Gamma_a(\Delta_a)A_{DFT}^{Surf} \right). \quad (3.4)$$

In equations 3.2-3.4: $E_{DFT}^{Bulk}(\Delta_a)$ is the DFT energy of the bulk Al system with applied displacement Δ_a . $E_{DFT}^{Surf+H}(\Delta_a)$ is the DFT energy of the periodic surface cell with a hydrogen impurity. A_{DFT}^{Bulk} and A_{DFT}^{Surf} are the areas of the slip/decohesion planes for the bulk and surface cells, respectively. $A^{3Layers}$ is the area of the slip/decohesion plane intersecting with the outermost 3 $\{111\}$ layers of aluminum atoms in the surface cell. In equations 3.3 and 3.4, $n = 2$ for decohesion and $n = 1$ for slip.

$E_{DFT}^{Surf+H}(\Delta_a)$ was calculated using the geometry described in figure 3.3a, which is a periodic cell with a $[111]$ surface oriented at an angle of 70.5° with respect to the slip/decohesion plane (also a $[111]$ plane). The utility of this simulation cell is that the $[111]$ component of the C cell vector (C_{111}) can be extended incrementally to impose decohesion at the $[111]$ A-B cell boundary. Similarly, the

[11 $\bar{2}$] and [110] components of the C cell vector ($C_{11\bar{2}}$ and C_{110}) can be changed to impose interatomic slip on the same plane.

Realistic surface relaxation was achieved in the initial configuration by allowing the outermost three layers of atoms to move freely to achieve a force convergence of 20.0 meV/. During each increment of slip (0.2 increments), all atoms within two layers of the slip plane were allowed to move freely in the direction normal to the cell boundary. For the decohesion calculation, only one displacement increment was performed ($\Delta_{dec} = 15$). In this case, all aluminum atoms within three layers of the free surface were allowed to move freely, while all others were held fixed. In all cases, the hydrogen impurity was free to move in any direction.

The values of $\Gamma'_{decohesion}$ for different hydrogen binding sites are presented in figure 3.3b. The plotted values represent the %-change relative to the hydrogen-free calculation for the same geometry. When located on the same plane as a newly forming surface (the decohesion plane), adsorbed hydrogen impurities significantly reduce the barrier for surface creation. Of the sites considered, the largest effect occurs when the hydrogen is located at a sub-surface site intersecting the decohesion plane. In this case, $\Gamma'_{decohesion}$ is reduced by 20% for the chosen geometry, suggesting that a much greater multiple of this effect may be possible if the decohesion plane is completely saturated with hydrogen. Although several binding sites result in a slight increase in $\Gamma'_{decohesion}$, the overwhelming trend is one of hydrogen enhanced decohesion. Thus, it is reasonable to expect a typical distribution of hydrogen impurities to decrease the barrier for surface formation at a free surface, and then also, at a loaded crack-tip.

Due to the computational expense of the Γ'_{slip} calculations, we only consid-

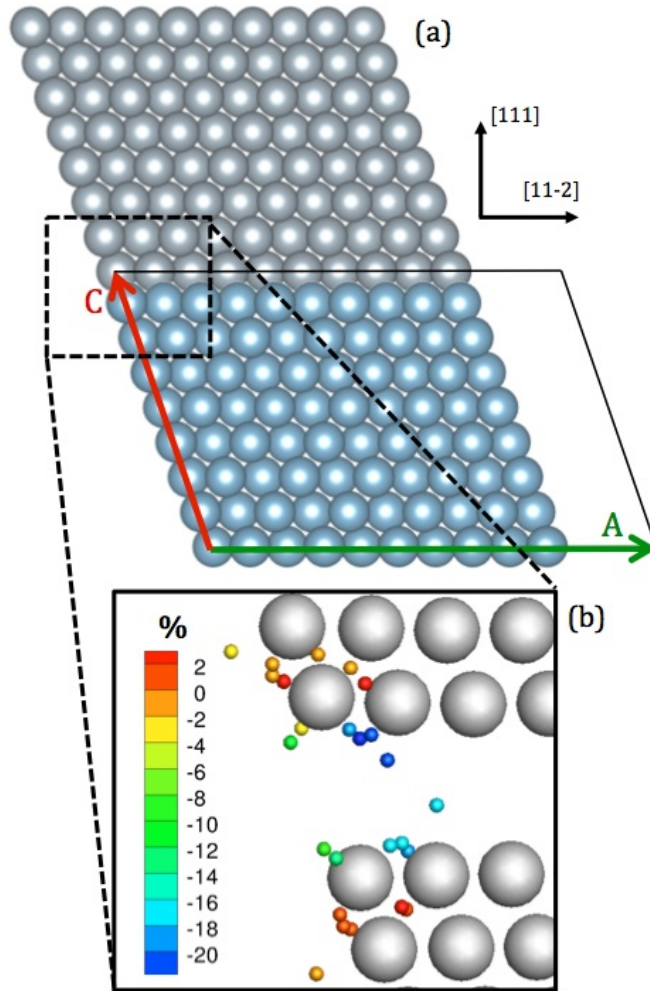


Figure 3.3: (a) The periodic simulation cell used to calculate $E_{DFT}^{Surf+H}(\Delta_a)$. The B cell vector (not shown) is perpendicular to the A-C plane, and pointing into the page. Note that both the A-B and B-C cell boundaries are in the $\{111\}$ family of planes. The grey atoms represent the next periodic image of the simulation cell in the C direction. (b) Summary of $\Gamma'_{decohesion}$ plotted on the imposed decohesion plane. Results are colored according to the %-change in $\Gamma'_{decohesion}$ relative to the hydrogen-free calculation for the same $\{111\}$ surface.

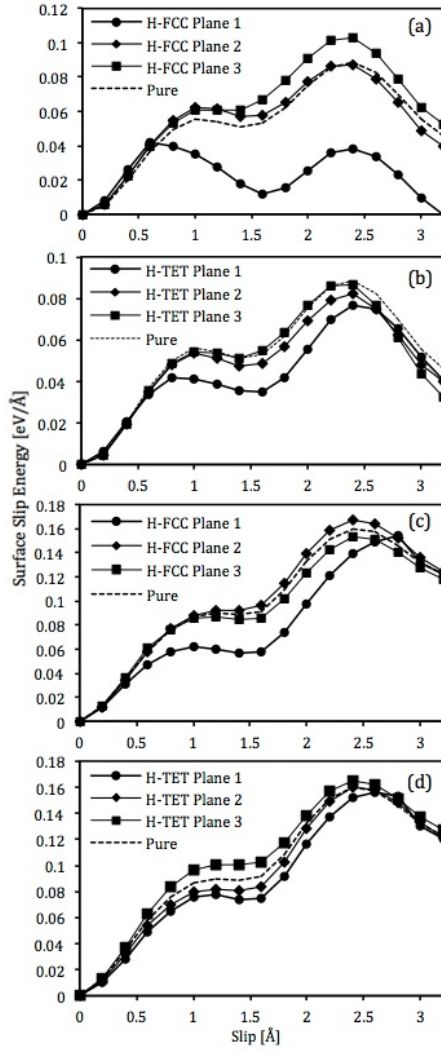


Figure 3.4: Plots of Γ'_{slip} for an aluminum surface with and without hydrogen. (a) and (b) show Γ'_{slip} for hydrogen in the fcc and first tetrahedral-B sites for ACUTE step formation, respectively. (c) and (d) depict Γ'_{slip} for hydrogen in the fcc and first tetrahedral-B sites for OBTUSE step formation, respectively. In each plot, the hydrogen-free calculation is plotted as a dashed line for reference, and the hydrogen binding site of interest was considered on three different atomic planes lying parallel to the A-B cell boundary. Plane 1 is on the A-B cell boundary, Plane 2 is on the next plane above the cell boundary and Plane 3 is on the next plane below the cell boundary.

ered hydrogen bonded at the FCC surface site and 1st tetrahedral-a sub-surface site when investigating slip. A detailed summary of these results is reported in figure 3.4. The effect of hydrogen was found to be most significant when the imposed slip produces an acute surface step at the A-B cell boundary. In this case, the isolated energy barrier for creating the surface step is much lower than when an obtuse step is formed (slip in the opposite direction). In either case, the presence of a single hydrogen impurity can either increase or reduce Γ'_{slip} for either a leading or trailing Shockley partial dislocation.

According to our own KS-DFT predictions and experimental measurements of hydrogens diffusivity in aluminum [62], one can expect atomized hydrogen to quickly move between interstitial sites at room temperature. For this reason, the mechanical behavior will be dominated by the weakest cases, when Γ'_{slip} is reduced; and thus, surface step formation can be expected to occur more frequently in the presence of hydrogen. When combined with the $\Gamma'_{decohesion}$ results already presented, the overall prediction is that hydrogen surface impurities will enhance both slip and decohesion activity at a $\{111\}$ aluminum surface at room temperature. Given this evidence, we propose that a combination of both AIDE and HEDE are responsible for regime (ii) HAC behavior in the form of the unified mechanism of hydrogen enhanced surface deformation (HESD).

3.5 Multiscale Fatigue Model: Setup

Both analytic and atomistic models have clearly demonstrated that a direct connection exists between material properties such as $\Gamma'_{cleavage}$ (or $\Gamma'_{decohesion}$) and a materials tendency for crack-tip cleavage (or dislocation emission) [63, 41].

However, such a connection has not been made between these parameters and near threshold fatigue crack growth rates. The challenge is that an appropriate model requires both atomistic resolution at the crack-tip and a large spatial domain for the emitted dislocations to glide away naturally.

Harnessing recent increases in computational resources, advanced multi-scale modeling, and a strategic bond shielding approximation (SBSA), we are now capable of addressing this challenge. To do so, we have employed a Coupled Atomistic and Discrete Dislocation (CADD) multiscale model consisting of an atomistic region at the crack-tip, embedded in a larger discrete dislocation continuum domain (figure 3.5). The coupling allows for dislocations to pass between the two regions following the approach introduced by Shilkrot et al. [47].

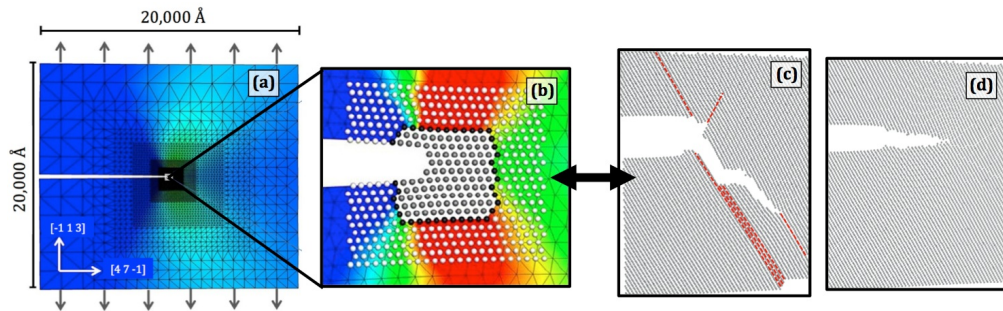


Figure 3.5: (a)-(b) CADD simulation setup, as discussed in the text and references [2, 47]. (a) Geometry of the continuum discrete dislocation domain, where boundary conditions are applied. (b) A simple embedded atomistic domain is shown for illustrative purposes. Behavior of grey and black atoms is defined by SBSA enhanced EAM molecular mechanics. Behavior of white atoms is interpolated from the elastic continuum displacements. (c)-(d) Typical crack-tip deformation mechanisms varied at low to moderately high growth rates. Here, we see that the same moderately high crack growth rate ($\sim 10/\text{cycle}$) can be a result of both slip band cracking and brittle cleavage. In (c), red dashed lines are used to highlight active slip planes.

Unless otherwise stated, all CADD-based simulations presented here were performed using the geometry and procedural details discussed by Baker and Warner [2]. The geometry consisted of a single crystal of fcc aluminum, oriented such that the horizontal axis corresponded with $[4\bar{7}1]$, the vertical axis with $[\bar{1}13]$, and the out of plane direction with $[2\bar{1}1]$. The explicit crack plane was created by removing three consecutive planes of atoms normal to the vertical axis, making the crack front aligned with the $[2\bar{1}1]$ direction. The $(\bar{1}11)$ slip plane intersected the crack plane at an angle of 58.5 degrees from the horizontal, with the $[011]$ slip direction in the xy plane. For the chosen geometry, the primary slip plane is the $(\bar{1}11)$ plane and the primary slip direction is the $[011]$ direction. All other slip planes are oblique to the xy plane, meaning the normal vector to the plane is not in the plane of the 2D continuum discrete dislocation (DD) region.

This orientation was chosen for two primary reasons. First, the line direction of full dislocations is normal to the crack front, meaning that there are no model thickness effects for the principal physical mechanisms. Second, the primary means of slip involves full dislocations that have pure edge character, consistent with the limitations of the model [2].

The crack tip was embedded into a 3D atomistic region of approximately $150 \times 150 \times 10 \text{ \AA}$, which was encompassed by a larger 2D plane strain, discrete dislocation continuum region spanning $2 \times 2 \times 0.001$ microns. The atomistic region is described by 0K molecular mechanics routine, using the interatomic potential for aluminum by Ercolessi and Adams [11]. In the continuum domain the anisotropic elastic constants, $C_{11} = 0.682$, $C_{12} = 0.331$, $C_{44} = 0.180 \text{ eV/\AA}^3$ were used, along with a cubic fcc lattice constant of 4.03208 \AA . Loads were applied

by prescribed displacements at the outer boundary of the continuum region corresponding to the continuum solution for a sharp crack in an anisotropic linear elastic material subjected to mode I loading. The interface updating in CADD was done during every atomistic (conjugate gradient) step.

All fatigue simulations used a maximum stress intensity (K_{MAX}) of $0.6 \text{ eV}/^{2.5}$ and a load ratio (R) of 0.25. The applied loading followed a typical fatigue saw-blade pattern consisting of 50 load step increments per fatigue load cycle. For each simulation, loading was applied until the crack had propagated into the atomistic domain boundary, or 10 load cycles had been reached.

While the atomistic domain was composed solely of aluminum atoms, a specific aluminum alloy was studied by choosing the appropriate dislocation glide resistance in the continuum domain [2]. To compare with the experiments of Ro et. al. [44], we chose to model an AA2x24 alloy, C433 aluminum (4.0 Cu, 1.4 Mg, 0.6 Mn, wt.%) with T351 aging conditions. Considering the reported uniaxial yield stress of $\sigma_y = 358 \text{ MPa}$ [16] and the GP zone hardening relationship discussed by Singh and Warner [49], a dislocation glide resistance of 110 MPa was used.

3.5.1 Strategic Bond Shielding Approximation (SBSA)

While the CADD approach makes the atomistic simulation of near threshold fatigue crack growth possible [2], the size and timescale of the required atomistic domain is still well beyond what is feasible with KS-DFT. Thus, an empirical interatomic potential approach is required. Here, we used a well-established aluminum-only potential [9] that has been shown to predict the crack-tip re-

sponse of pure aluminum in accordance with DFT predictions [33, 18].

In order to capture the effect of hydrogen on $\Gamma'_{cleavage}$ and $\Gamma'_{decohesion}$ within the multiscale model, the EAM bonding description was modified according to the SBSA procedure presented here. At the start of each load increment, the number of allowed shielding events for that step (n) was chosen by the summation $\Sigma(R_i < p_H)$ from $i = 1$ through 10. Here, R_i is a list of random numbers (0-1) and p_H is one tenth of the probability that a shielding event will be allowed to occur at a given load step. A continuous distribution of p_H input parameters was used to produce an approximately continuous distribution of environmental exposure results.

The SBSA technique works by identifying critically stretched bonds of surface aluminum atoms, and then shielding a number of these bonds that is proportional to the environmental exposure level until a new equilibrium configuration is found. Here, this technique was implemented using the following procedure:

1. Using a force gradient routine, allow all free atoms to relax to their equilibrium positions.
2. Determine if each atom is on the surface by taking the ratio between its 1st and 12th nearest neighbor distance.
3. For all atoms near the surface, any di-atomic force contribution greater than the critical di-atomic force parameter (f_{bar}) is stored in a descending list.
4. Assuming n shielding events are allowed, n unique atoms are chosen from the descending list.

5. Once an atom is targeted for a shielding event, that atoms critical bonds are completely shielded by cancelling the diatomic forces. The forces are continuously cancelled until the system reaches equilibrium.
6. Once an atom is targeted for a shielding event, that atom is prevented from experiencing any force contribution greater than f_{bar2} for the remainder of the simulation.

To chose appropriate parameters for the SBSA procedure, we repeated the $\{111\}$ Γ' calculations with the following modifications: (1) EAM+SBSA was used to calculate forces in lieu of KS-DFT, (2) all atoms were held fixed during the decohesion/slip simulation, (3) a simple force integration procedure was used to determine the total energy at each deformation step, and (4) a single shielding event was allowed, lasting for the entire slip/decohesion simulation once activated.

Considering the mobility of atomic hydrogen, the SBSA parameters were fit to reproduce the KS-DFT predictions in which hydrogen most decreased Γ' . Specifically, we chose the SBSA parameters, f_{bar} and f_{bar2} , that resulted in the following changes in the Γ' barriers for the three cases: the formation of a partial acute step $\approx -25\%$, the formation of a partial obtuse step $\approx -28\%$, and full decohesion $\approx -20\%$. We found that these conditions were best accomplished by setting $f_{bar} = 0.05\text{eV}^{-1}$ and $f_{bar2} = 0.025\text{eV}^{-1}$. Using these parameters, the acute step, obtuse step and decohesion barriers were decreased by approximately -25% , -20% and -18% , respectively.

Although the fit SBSA parameters (above) were used for the CADD results presented in figure 3.6, simulations were also performed with slightly larger SBSA parameters ($f_{bar} = 0.06\text{eV}^{-1}$ and $f_{bar2} = 0.03\text{eV}^{-1}$). These results were not

qualitatively distinguishable from those presented here, and thus, we assert that the CADD predictions are relatively insensitive to the exact choice of the SBSA parameters.

3.6 Multiscale Fatigue Model: Results and Discussion

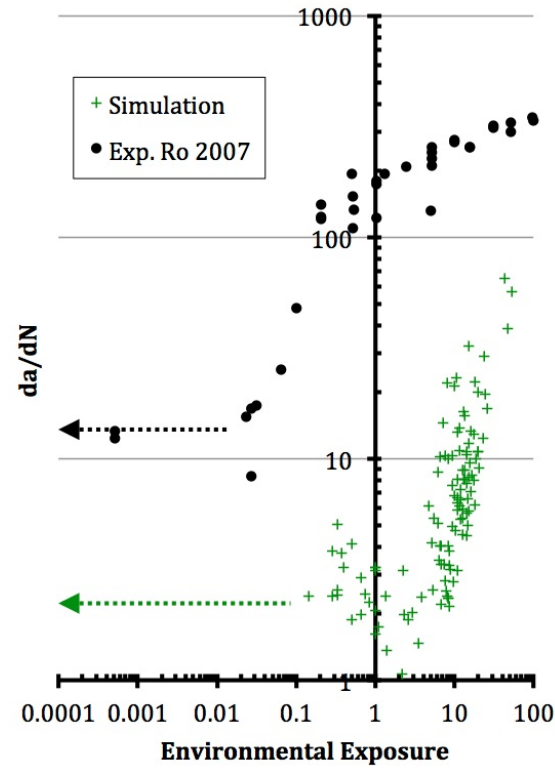


Figure 3.6: Comparison of CADD simulation results with experimental fatigue data for a C433 aluminum alloy. Units for crack growth rate, da/dN , are /cycle. For simulation data points (shown in green), environmental exposure is in units of average number of allowed shielding events per load cycle. For experimental data points (shown as black circles, obtained from reference [44]), environmental exposure is in units of $Pa \cdot s$. The horizontal green and black dashed arrows show the approximate growth rates in vacuum for simulation and experiment, respectively.

To account for the statistical nature of hydrogen enhanced crack growth, we performed a set of 125 CADD fatigue simulations, with various levels of environmental exposure. In order to plot both the simulation and the experimental data on the same plot in figure 3.6, we use the assumption of Ro et. al. [44] that the P/f measurement of environmental exposure is proportional to the number of hydrogen impurities available to react with the exposed crack-tip in the regime of interest. Accordingly, we define the environmental exposure level in the simulations by the average number of shielding events that occurred during each load cycle. This value is expected to be proportional to, but not equal to, the P/f exposure levels reported by Ro et. al. [44].

As was observed in experimental studies by Ro [44] and Wei [59], varying the environmental exposure level in the CADD simulations led to variation in both the crack growth rate (da/dN) and number of dislocations present at the crack-tip. Altogether, four major trends were observed in the simulations. The first and most obvious of these trends being that the average crack growth rate increases as the exposure level increases. The second major trend is the existence of a threshold environmental exposure level, T_{Exp} , below which the first trend ceases to exist. We find an upper bound for the threshold exposure level at approximately 6.8 hydrogen events per load cycle by noting that all da/dN predictions are greater than the exposure-free growth rate above this value. The exposure-free growth rate was obtained by running CADD without the SBSA procedure. This value is shown as a green dashed arrow in figure 3.6.

While the first and second trends describe variation in da/dN , the third and fourth describe the competition between cleavage and plastic slip via dislocation emission at the crack tip. The third trend being that there was very lit-

the plastic slip observed in simulations with the highest recorded growth rates ($da/dN > 20$ /cycle). In other words, when many shielding events are allowed (lots of hydrogen present), the crack-tip tends to deform by creating new surfaces rather than nucleating dislocations. The fourth and final trend is that the competition between cleavage and dislocation emission behavior becomes much more variable at lower da/dN levels. Even for simulations resulting in moderately high growth rate predictions ($da/dN = 10$ /cycle), there is strong variability in the number of dislocations observed. For example, figures 3.5c and 3.5d show two situations with similar da/dN measurements, but very different deformation behavior.

Overall, the da/dN vs exposure predictions shown in figure 3.6 are in strong agreement with the data from Ro et. al. [44]. Both the simulation data presented here and the referenced experimental study predict that C433 aluminum will exhibit an exposure threshold followed by a proportional increase in da/dN as the exposure continues to grow. In figure 3.6, the absence of a T_{Sat} threshold for the simulation data should be expected. As discussed, the ability to capture this threshold requires an explicit model of oxidation at the crack tip, which has been left for future study.

The small translation disagreement between simulation and experimental data should also be expected. The application of different (yet proportional) units for the environmental exposure level obviously explains a translational shift between simulation and experimental T_{Exp} predictions. Additionally, the crack growth rates measured in simulations are expected to be less than those observed in experiments because: (1) we have excluded possible secondary HAC mechanisms and oxidation effects, and (2) we have simulated a single

crystal with a very small out-of-plane dimension and no initial plastic shielding; yielding an expected fracture toughness less than the experimental value, thus requiring the application of a lower fatigue load (K_{MAX}) than the one used in reference [44].

3.7 Conclusion

In summary, we have started with an *ab initio* study of hydrogen binding at an aluminum surface, and subsequently worked out the expected effect a surface impurity should have on slip and decohesion. This information was used within a concurrent atomistic-continuum multiscale framework to directly predict the fatigue behavior of a C433 aluminum alloy in the presence of an environment with variable humidity. All details considered, the strong qualitative agreement between simulation and experimental trends is evidence that HESD could be the controlling failure mechanism for precipitate hardened aluminum alloys at regime (ii) environmental exposure levels. Furthermore, this direct, physics based prediction of real HAC behavior is a valuable step in the ongoing effort towards physics based failure modeling in the engineering world.

CHAPTER 4
NEAR-THRESHOLD FATIGUE LOADING IN ALUMINUM AND THE
MECHANICAL EFFECTS OF MONOLAYER SURFACE-LAYER
STIFFENING

4.1 Abstract

We utilize a concurrently coupled atomistic and discrete dislocation multiscale method (CADD) to directly simulate crack-tip deformation and propagation during near-threshold fatigue loading in aluminum. The effects of environmental monolayer surface-film stiffening are investigated by adding a Lennard-Jones overlay potential to exposed aluminum crack-face atoms. For the single crystal orientation studied here, we find that deformation behavior generally begins with a short period of fast transient crack-tip propagation until a stable defect structure has formed ahead of the crack-tip. During all stages of fatigue loading, highly irregular crack-growth behavior is observed. The approximate effects of stiff monolayer surface-film formation are found to significantly inhibit the initial crack growth rate by resisting typical slip-plane cracking behavior. Beyond the initial stage of transient propagation, surface layer stiffening continues to inhibit crack-growth behavior, but to a lower and less certain degree. The results are discussed in terms of the current fatigue literature and insights are provided for future work.

4.2 Introduction

Due to their excellent strength-to-weight ratio and natural resistance to corrosion, aluminum alloys have been used in lightweight aircraft structures for more than a century. As these alloys continue to serve as a primary material system, a key design concern involves the prediction of fatigue crack-growth (FCG) based failure, i.e. the propagation of crack defects under cyclic subcritical loading. Despite decades of research on the phenomenon of fatigue in structural metals [55, 43, 38], the specific atomistic mechanisms governing the onset of slow crack-tip propagation at the so-called fatigue threshold remain unclear. Although many well-received theories and supporting empirical models have been formulated through direct observation [43, 37], the length and time-scale limitations of current experimental capabilities make it difficult to distinguish correct theories from phenomenological approximations.

At this time, the most promising path to a comprehensive understanding of near-threshold fatigue is likely through direct, physics-based, atomistic simulation. Unfortunately, many significant challenges tend to prevent researchers from producing atomistic models capable of capturing true fatigue mechanisms in real alloys. One such challenge is the production of simulations with appropriately sized spatial domains. The application of small spatial domains can artificially influence the glide of dislocations away from the crack-tip, affecting long-range boundary conditions and ultimately biasing crack tip behavior [12, 13, 17]. A common solution to this issue is the application of a discrete dislocation (DD) dynamics model [10]. While DD simulations are much cheaper to scale, these models do not explicitly represent the atomic scale complexities that occur at a crack-tip, and thus cannot fully capture the microscopic mechanisms

of interest.

In addition to the spatial-scale challenge present in direct fatigue modeling, it is also difficult to produce simulations capable of incorporating realistic environmental effects. That is, typical atomistic simulations often rely on the approximation of an inert chemical environment [12, 13, 58, 17, 61]. Due to the well-known formation of a native oxide film on oxygen-exposed aluminum surfaces [25], a thorough atomistic study of fatigue in aluminum alloys must consider the possible micro-mechanical effects of surface-film formation.

Here we take steps in resolving the aforementioned challenges by using a concurrently coupled atomistic and discrete dislocation multiscale framework (CADD) [47, 8, 48, 34, 63, 2]. While the use of CADD is intended to reduce the computational demands required to model an appropriate sized atomistic domain, we also approximate the mechanical effects of stiff monolayer surface film formation using a Lennard-Jones [20] overlay potential to modify the behavior of exposed aluminum crack-face atoms. This approach is intended to approximately mimic the general surface-stiffening behavior experienced during oxygen monolayer coverage. Such an occurrence is expected during the early stages of oxide formation [25]. While this approach does not allow for the direct quantification of explicit aluminum oxide surface film effects, it does allow for a reasonable sampling of possible qualitative crack-tip deformation and propagation trends.

4.3 Background

Although it is well known that aluminum alloys rapidly form aluminum oxide surface films in the presence of environmental oxygen, it remains unclear exactly how oxide film formation affects crack-tip propagation behavior. When the cyclical crack growth rate ($\frac{da}{dN}$) is high in a vacuum environment, experimental studies have shown that crack-tip propagation behavior does not change when dry oxygen gas is added to the system [52]. While this trend might be a consequence of the large fatigue process zone present at high loads, it may also be that the crack-tip is propagating more quickly than the oxygen environment is transported. At near-threshold fatigue levels, when molecular transport is not an issue, multiple experimental studies have shown that a dry-oxygen environment can accelerate the average growth rate [52, 6, 5]. However, it is possible that the ample time allowed for molecular transport may also be enough time for trace levels of hydrogen to reach the fatigue process zone, and embrittle the material [52, 6, 5, 44].

Given that the true effects of a dry-oxygen environment on fatigue crack-growth are ultimately unclear, this work is intended to provide further insight through direct atomistic simulations. The overall goals are to (1) characterize the deformation behavior of an aluminum crack-tip during near-threshold loading, and to (2) determine the micro-mechanical effects of monolayer surface film stiffening.

4.4 Methods

The CADD-based model presented here was designed to directly capture cyclical crack-tip deformation behavior on the atomistic scale. The focus of the model is a small molecular mechanics domain used to encompass the tip of an ultra-sharp crack-tip in aluminum. Surrounding this atomistic domain, a larger continuum domain is used to apply boundary conditions via finite element analysis and to allow dislocations to glide away from the loaded crack-tip via dislocation dynamics (DD).

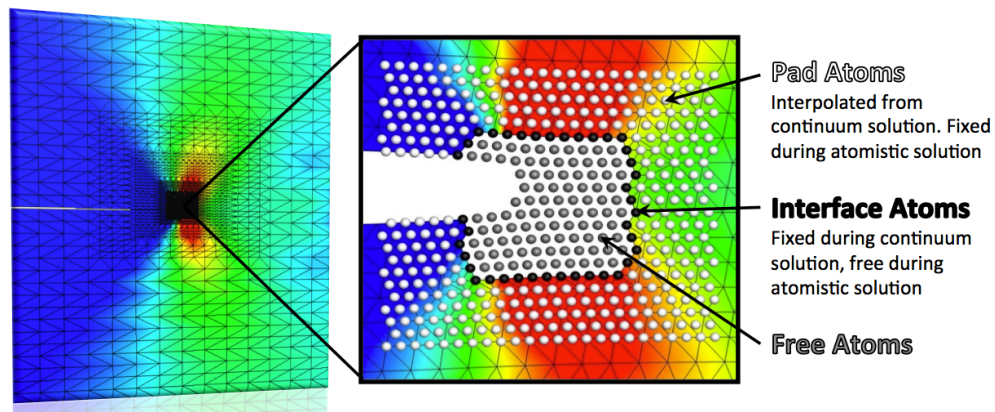


Figure 4.1: Illustration of the CADD multiscale methodology, as discussed in the text and references [2, 47, 8, 48]. The left-hand image shows the geometry of the continuum discrete dislocation domain, where boundary conditions are applied. The right-hand image shows an atomistic domain, which has been miniaturized for illustrative purposes. For the simulations presented in this work, the behavior of grey and black atoms are defined by embedded atom model (EAM) molecular mechanics. Behavior of white atoms is interpolated from the elastic continuum displacements.

4.4.1 Multi-scale Framework: Coupled Atomistic and Discrete Dislocations (CADD)

The coupling methodologies used within the crack-tip model were built upon the CADD techniques of Shilkrot et al [47]. The underlying framework consists of solving problems in two distinct domains, coupled by self-consistent displacement boundary conditions. As illustrated in figure 4.1, these domains include an atomistic region bounded by a set of interface atoms/nodes, and a continuum DD region approximated by linear elastic finite elements. In addition to these two domains, an additional layer of pad atoms is used to bound the interface atoms, and overlap with the continuum domain. Altogether, the pad atoms serve two critical purposes. First, they prevent a non-physical free surface from existing along the interface atom boundary. Second, they serve as a fixed boundary condition during relaxation within the atomistic domain.

A smooth transition in elastic deformation is achieved between the continuum and atomistic domains by switching between the use of interface atoms and pad atoms as fixed boundary conditions. While the interface atoms serve as a fixed boundary during all continuum solutions, the pad atoms serve as a fixed boundary during all atomistic solutions. In contrast to the atoms located within the immediate atomistic domain, the positions of the pad atoms are determined directly by the continuum solution alone. Thus the pad atoms provide the necessary non-local boundary conditions across the interface to the atomistic and DD regions.

Within the continuum region, the position of each node is a local function of the boundary conditions and the resulting deformation within that region. The

continuum region is assumed to be in a constant state of static equilibrium, such that the energy functional associated with the region is always minimized in the form:

$$E^C = \frac{1}{2} \int_{\Omega_C} (\hat{\sigma} + \tilde{\sigma}) : (\hat{\epsilon} + \tilde{\epsilon}) dV - \int_{\partial\Omega_T} T_o(\hat{u} + \tilde{u}) dA, \quad (4.1)$$

where Ω_C represents the continuum domain and Ω_T represents the boundary of the continuum domain on which a traction boundary condition, T_o , exists. $\tilde{\sigma}$, $\tilde{\epsilon}$, and \tilde{u} represent the infinite medium stress, strain, and displacement fields, respectively, for the discrete dislocations at their distinct locations. $\hat{\sigma}$, $\hat{\epsilon}$, and \hat{u} represent the solution fields from an anisotropic linear elastic boundary value problem that when superimposed with the dislocation fields satisfy the overall boundary conditions. $\hat{\sigma}$, $\hat{\epsilon}$, and \hat{u} are obtained using a standard displacement based finite element approach, while $\tilde{\sigma}$, $\tilde{\epsilon}$, and \tilde{u} are established analytic fields. For a more in-depth overview of the CADD modeling procedures, including the details of inter-domain dislocation passing and continuum DD theory, the reader can find more information in publications by Shilkrot et al. [47] as well as Baker and Warner [2].

Surface Film Effects: LJ+EAM

In order to approximate the mechanical effects of stiff monolayer surface film growth. A Lennard-Jones [20] pair potential is used to magnify the inter-atomic forces between exposed aluminum crack-face atoms. For specifically chosen surface atoms, this effect is achieved by adding a pairwise Lennard-Jones interaction to the EAM potential governing all other atoms in the system. The addition of this secondary Lennard-Jones pair potential is referred to here as an overlay potential. When applied to every atom within a 4x4x4 cubic FCC su-

		EAM	EAM+LJ	LJ Effect
C_{11}	[Gpa]	118.87	385.08	+224%
C_{12}	[Gpa]	62.879	214.12	+241%
C_{44}	[Gpa]	32.972	184.30	+459%
Y_{us}	[eV/Å ²]	0.0106	0.0390	+267%
$Y_{surface}$	[eV/Å ²]	0.0569	0.1693	+198%

Table 4.1: Mechanical properties of aluminum supercell with and without a Lennard-Jones overlay potential applied to all atoms. The parameters of the overlay potential were chosen to increase all parameters listed in table 4.1, and to produce an increase in C_{44} roughly comparable to a transition from Al to Al_2O_3 (450-500%). The parameters were also chosen so as to leave the FCC lattice constant effectively unchanged.

percell, the chosen Lennard Jones parameters used within the overlay potential result in an overall stiffening of the system. The changes in specific mechanical properties produced by the addition of the overlay potential are summarized in table 4.1.

In order to track crack-tip propagation and to detect surface atoms during run-time, a simple volume grid approach is utilized, as illustrated in figure 4.2. At the beginning of each load step, the status of each cell in the static volume grid is labeled as either a free-space or solid cell. A cell is labeled as a free-space cell if it is adjacent to eight cells containing zero aluminum atoms, and is also empty. Once the free-space and solid cells have been determined, the surface atoms are detected by locating all atoms within two cells of a free-space cell. This allows the crack-tip position to be tracked by locating the furthest surface atom from the initial crack-tip location in the positive x-direction. For the simulations presented here, each cell in the volume grid was set to be 1.5 x 1.5 Å in the x and y-directions, and to be the entire atomistic region thickness in the z-direction.

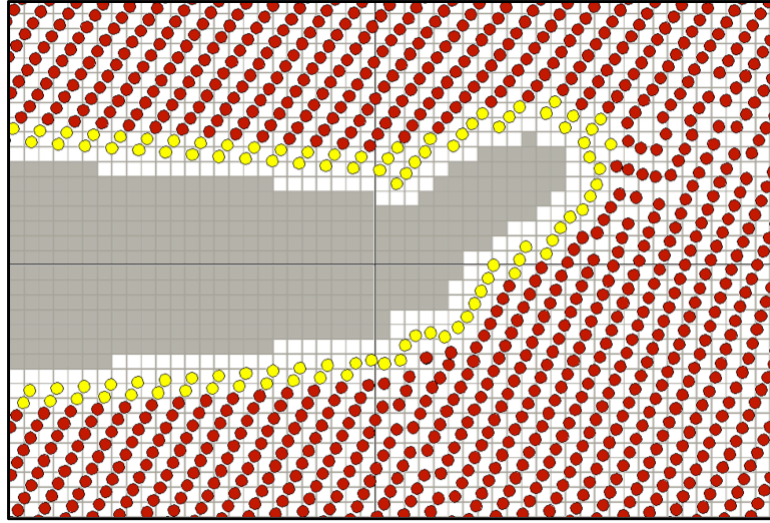


Figure 4.2: An illustration of the volume grid used to track crack-tip propagation and detect surface atoms for adding an overlay potential. Free-space volume grid cells are shaded in gray, while solid cells are white. Surface atoms experiencing overlay potential effects are showed in yellow, while all other atoms are shown in red.

During fatigue simulations in which stiff monolayer surface stiffening was considered, n_{ML} exposed surface atoms were randomly selected at the start of each load step for the addition of an overlay potential for the remainder of the simulation. Here, n_{ML} is the number of atoms with potentials that need to be modified, and it is equivalent to $(n_S \Theta_{ML} - n_F)$, where n_S is the number of currently exposed surface atoms (both modified and unmodified), n_F is the number of exposed surface atoms already experiencing overlay effects and Θ_{ML} is the desired monolayer coverage required for the current load step. In all simulations considering monolayer film effects, Θ_{ML} was linearly interpolated between 0 at $K_I = 0$ and 1.0 at $K_I = K_{MAX}$, where K_I is the current mode I stress intensity and K_{MAX} is the maximum stress intensity expected during load cycling. The same relationships were used in simulations meant to approximate in-vacuo conditions, however Θ_{ML} was linearly interpolated between 0 at $K_I = 0$ and 0.1

at $K_I = K_{MAX}$. Although a true in-vacuo simulation would require that $\Theta_{ML} = 0$ at all times, the small value used here was designed to introduce statistical variability to the system. Without this variability, the deterministic nature of zero-temperature simulations would have prevented the macroscopic averaging analysis presented later.

4.4.2 Multi-scale Fatigue Model Setup

In all simulations, the model geometry consisted of an FCC aluminum crystal, oriented such that the horizontal axis corresponded with $[4\bar{7}\bar{1}]$, the vertical axis with $[\bar{1}13]$, and the out of plane direction with $[2\bar{1}1]$. An explicit crack plane was created by removing three consecutive planes of atoms normal to the vertical axis, making the crack front aligned with the $[2\bar{1}1]$ direction. For this orientation, a $(\bar{1}\bar{1}1)$ slip plane intersects the crack plane at an angle of 58.5 degrees from the horizontal, with the $[011]$ slip direction lying on the xy plane. In all simulations, this $(\bar{1}\bar{1}1)$ plane is the dominant location of long-range slip. This orientation was chosen so that the line direction of full dislocations is normal to the crack front, and so that the primary means of slip involve full dislocations that have pure edge character, consistent with the limitations of the underlying model [2].

The explicit crack-tip was modeled within a 3D atomistic domain of approximately $25 \times 25 \times 1$ nm, as detailed in figure 4.3. This atomistic domain was then embedded within a larger 2D continuum region spanning 2×2 microns. The motion of atoms within this region was governed by a 0K molecular mechanics energy minimization routine using the Large-scale Atomic and Molecular Mas-

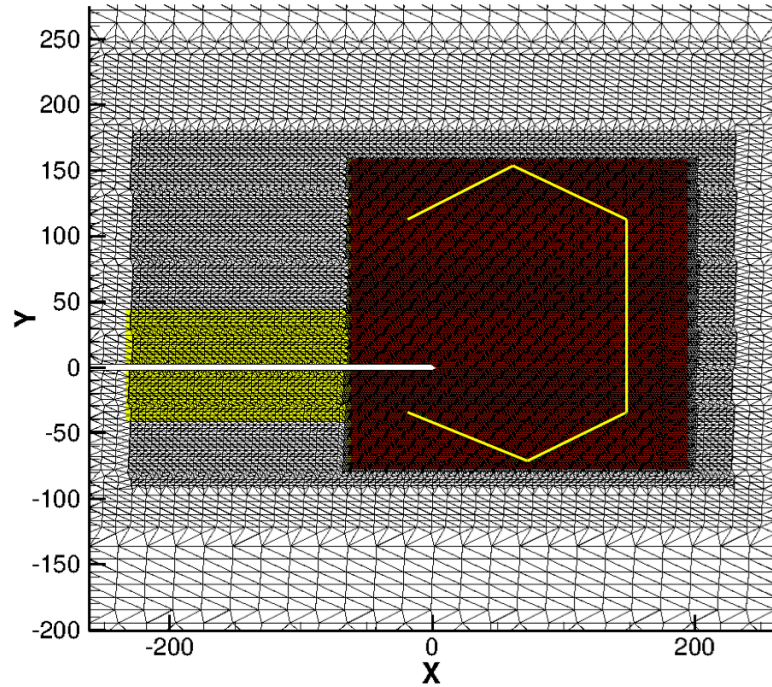


Figure 4.3: A snapshot of the actual atomistic domain and surrounding continuum mesh. The region highlighted in red is the mesh corresponding to the free and interface atoms modeled by EAM molecular mechanics (pad atom nodes are not shown to be overlapping with the courser continuum domain). The region highlighted in yellow shows the area along the continuum crack surfaces where the crack-tip opening distance is calculated at a constant distance from the current crack-tip location. Finally, the yellow line drawn over the red atomistic region shows the band of atoms where dislocations are detected and passed to the continuum domain. The details of dislocation passing are discussed in references [2, 47].

sively Parallel Simulator (LAMMPS) [39] as a dynamic library within a parallel multiscale wrapper code. The interatomic potential by Ercolessi and Adams [11] was used to calculate all inter-atomic forces during minimization. In the continuum domain the anisotropic elastic constants, $C_{11} = 0.682$, $C_{12} = 0.331$, $C_{44} = 0.180 \text{ eV}/\text{\AA}^3$, along with a cubic FCC lattice constant of 4.03208 \AA .

Loading was applied to the multiscale model by prescribing fixed displace-

ments at the outer boundary of the continuum region corresponding to the analytical solution for a sharp mode I crack in an anisotropic linear elastic material. The crack-tip position was updated at the start of every load step, and the interface updating in CADD was done after every other atomistic energy minimization step.

In all cases a fatigue load ratio, R , of 0.5 was used along with a stress intensity load ranges, ΔK , of 0.275, 0.300 and 0.325 eV/ $\text{\AA}^{2.5}$. The cyclical loading schedule followed a typical fatigue saw-blade pattern consisting of 44-52 load step increments per fatigue load cycle at a load step increment of ± 0.0125 eV/ $\text{\AA}^{2.5}$. For each simulation, loading cycling was applied until 15 fatigue cycles had been reached. For simulations at $\Delta K = 0.275$ eV/ $\text{\AA}^{2.5}$, additional simulations were run (with and without monolayer effects) for 32 load cycles.

While the atomistic domain was composed solely of aluminum atoms, the properties of a typical precipitation hardened aluminum alloy was approximated by choosing an appropriate dislocation glide resistance in the continuum domain [2]. Utilizing the hardening relationship discussed by Singh and Warner [49], it was determined that a continuum dislocation glide resistance of 110 MPa was reasonable approximation for a GP zone hardened alloy with uniaxial yield stresses reported to be roughly $\sigma_y = 358$ MPa [16].

4.5 Results

The multitude of multiscale fatigue simulations performed here exhibited three general trends for the geometry, temperature and loading details considered. First, fatigue behavior commences with a short period of fast transient crack-

tip propagation lasting between one and five load cycles. This period of fast propagation generally slows once a stable defect structure is accumulated ahead of the crack-tip. Second, within an isolated fatigue simulation, crack growth is highly irregular and discontinuous. Third, the approximate effects of stiff surface layer formation result in a reduction in dislocation nucleation as well as overall crack growth rates. However, the disparity between crack growth rates seems to decrease as more fatigue cycles are considered.

4.5.1 Transient Behavior

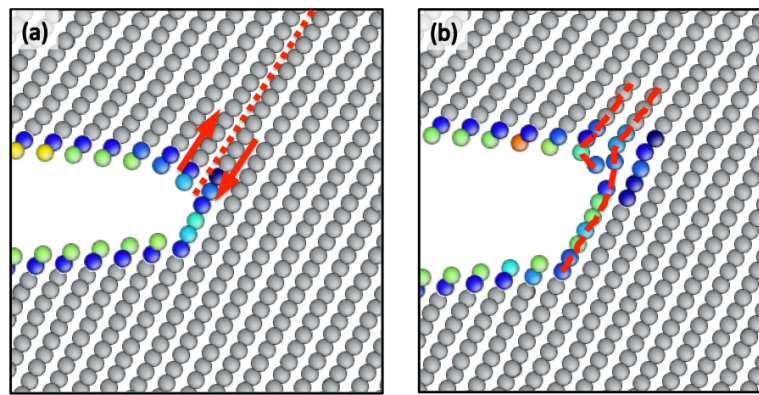


Figure 4.4: The first major deformation event experienced in the majority of simulations is dislocation nucleation from the primary slip plane intersecting the crack front. (a) Shows the nucleation of a dislocation along the primary slip plane (labeled with a dashed line). (b) Continued dislocation nucleation of the primary slip plane leads to a localized disordering of atoms to accommodate shear-tension coupling along the surface. To highlight the defect structures, atoms with non-FCC coordination are colored, while FCC atoms are grey.

The deformation and propagation of a pristine crack-tip in a single crystal of aluminum was found to begin with a transient period of fast crack growth lasting one to five fatigue cycles. Although the addition of a surface-film stiffening

had a significant effect on the magnitude of this transient stage of growth, all simulations exhibited similar behavior. In all cases, this fast propagation stage was controlled by the rapid nucleation of dislocations from the initially dislocation free crack-tip. In the majority of these simulations, the first sign of plastic deformation was the nucleation of one or more full dislocations along the primary slip plane intersecting the crack plane at 58.5 degrees. As illustrated in figure 4.4, the continued nucleation of dislocations along this plane eventually leads to the formation of a small immobile defect structure, usually resulting from shear-tension coupling along the surface. These defect structures generally lead to an increment of brittle failure, followed by further accumulation of defects ahead of the crack-tip. The fast propagation stage ends once the defect structure is large enough that it remains stable for multiple load cycles, temporarily arresting crack growth.

The magnitude of crack-growth experienced during the initial transient stage of fatigue deformation is most closely related to the number of consecutive dislocations allowed to glide away from the surface on the same slip plane, sharpening the crack-tip and localizing brittle defect structures in a small region of high stress concentration. As is illustrated in figure 4.5 for vacuum conditions, the emission of dislocations out of the atomistic region is most prevalent during the early transient stages of fatigue loading, and becomes less common once a stable defect structure forms and the fatigue loading progresses. Once a stable immobile defect structure has formed ahead of the crack-tip, propagation ceases to occur by slip-band cracking, and begins to occur by the gradual reordering and formation of trapped defect ahead of the crack.

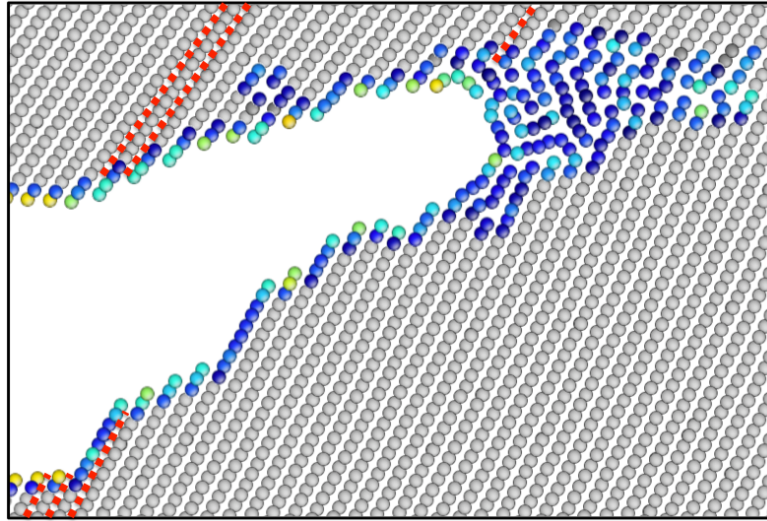


Figure 4.5: An in-vacuo fatigue simulation shown after 15 fatigue cycles. Red lines are used to label planes on which a full dislocation has nucleated and glided away from the surface. To highlight the defect structures, atoms with non-FCC coordination are colored, while FCC atoms are grey. It is clear that the majority of dislocation nucleation occurs during the early stages of deformation when crack growth is the fastest.

4.5.2 Irregular Propagation

During all observed stages of fatigue crack-tip deformation, propagation behavior is highly irregular and discontinuous. For a single fatigue simulation, the crack-tip does not advance by a fairly regular distance during each loading cycle. For example, a crack-tip defect structure may remain fairly stationary for 14 cycles, and then suddenly become reordered during the 15th cycle, advancing the crack-tip forward by a nanometer or more. This detail makes near-threshold fatigue crack growth difficult to quantify on an atomistic scale, because continuous crack-growth rates $\frac{da}{dN}$ cannot be directly extracted over a small number of load cycles. For the results presented here, $\frac{da}{dN}$ measures have been determined under the assumption that experimentally observable crack-growth behavior

can be approximated by a macroscopic ensemble average of many microscopic crack-tip responses. Unless otherwise stated, all plotted curves depicting the crack-tip position as a function of the fatigue loading cycle were determined by averaging the results of fifteen distinct simulations.

4.5.3 Surface Film Effects

The fatigue simulation results with and without the consideration of monolayer surface film stiffening are summarized in figure 4.6. After fifteen load cycles, it is clear that an in-vacuo crack is likely to propagate further than a crack with stiffened surface bonds. The primary cause of this disparity is the inhibition of early dislocation nucleation from the stiffened surface. As illustrated in figure 4.7, the presence of stiffened surface atoms tends to prevent dislocations from both initiating and gliding away from the crack-front and subsequently prevents slip-band cracking during the initial stage of fast transient propagation.

While the averaging of fifteen simulations for each curve provided reasonably smooth trends at $\Delta K = 0.275$ and $0.325 \text{ eV}/\text{\AA}^{2.5}$, the averaged curve for in-vacuo conditions at $\Delta K = 0.300 \text{ eV}/\text{\AA}^{2.5}$ still reflects some of the irregular crack-tip propagation behavior observed during isolated simulations. Even so, all results reflect the relatively intuitive trend that stiff monolayer formation is likely to inhibit slow crack propagation.

Although it is clear that cracks initially grow at a slower rate in the presence of stiffened surface bonds, the effect becomes slightly less significant and more uncertain as the load cycling continues. In figure 4.8, the approximate post-transient crack growth rates are quantified at $\Delta K = 0.275$ and $0.325 \text{ eV}/\text{\AA}^{2.5}$ for

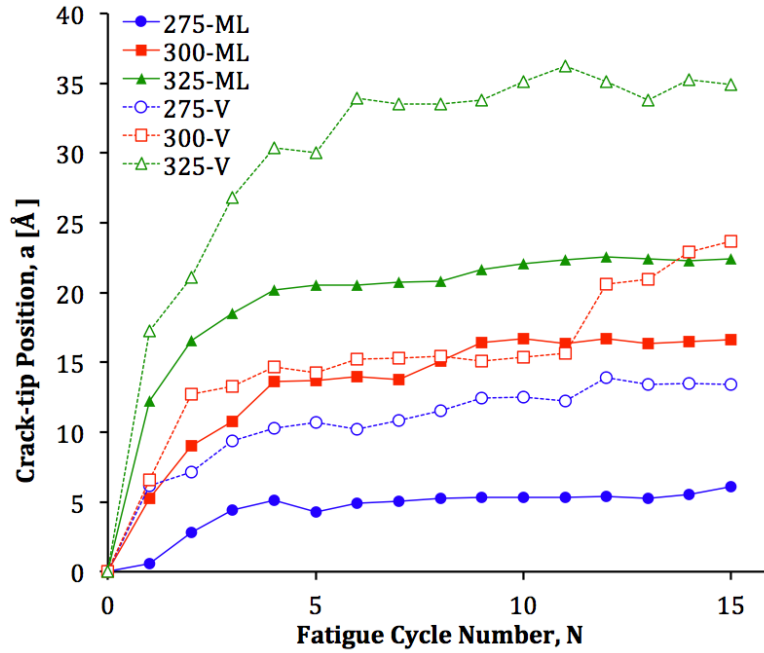


Figure 4.6: Curves depict the average location of the crack-tip for each fatigue load-range considered as a function of the current load cycle number. Loads listed in legend have units of $meV/\text{\AA}^{2.5}$. In legend, *V* denotes in-vacuo results, while *ML* denotes monolayer surface stiffening results.

in-vacuo and surface-film conditions. It is clear that the slopes are still higher for in-vacuo conditions. However, there is also more error in fitting relative to the small slopes that are the subject of comparison.

In order to provide more data for the collection of a post-transient crack growth rate, additional simulations were performed for both in-vacuo and monolayer surface film conditions at $\Delta K = 0.275 eV/\text{\AA}^{2.5}$ for 32 load cycles. As shown in figure 4.9, these longer simulations result in a slight increase in variability, and a decrease in the fitted crack growth rates. However, the disparity between in-vacuo and surface-stiffened growth rates is still present, albeit to a lesser degree.

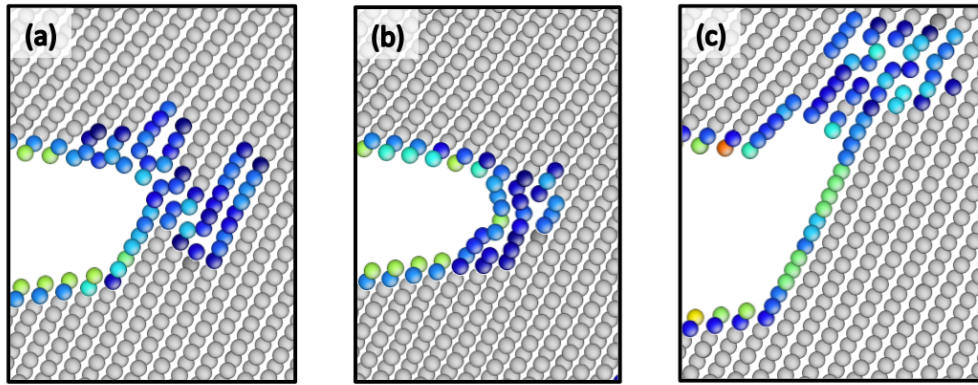


Figure 4.7: During the early stages of crack-tip deformation and propagation, stiff surface film formation clearly inhibits the nucleation of dislocations along the primary slip plane. (a) & (b) Show crack-tips with stiff monolayer surface film coverage after two full load cycles. (c) Shows an in-vacuo crack-tip after the same loading has been performed.

4.6 Discussion

The presented results provide several valuable insights regarding the direct simulation of atomistic-scale fatigue crack growth in aluminum. The most critical insight to consider before future research is performed is the necessity of a large atomistic domain. Although the use of a multiscale-model dramatically reduces the spatial requirements for producing accurate boundary conditions and avoiding boundary effects on dislocation behavior, there are still other details to consider. First, under cyclical fatigue loading, a sharp dislocation-free crack-tip will commence with a transient stage of fast crack-propagation. Thus, the atomistic domain must be large enough to capture this initial crack-tip advance by utilizing a large atomistic domain, or by implementing a model with an adaptive geometry. Second, a relatively large defect structure is formed at the crack-front by the end of the transient propagation stage. These defect structures were not observed in a predictable manner until large atomistic domains

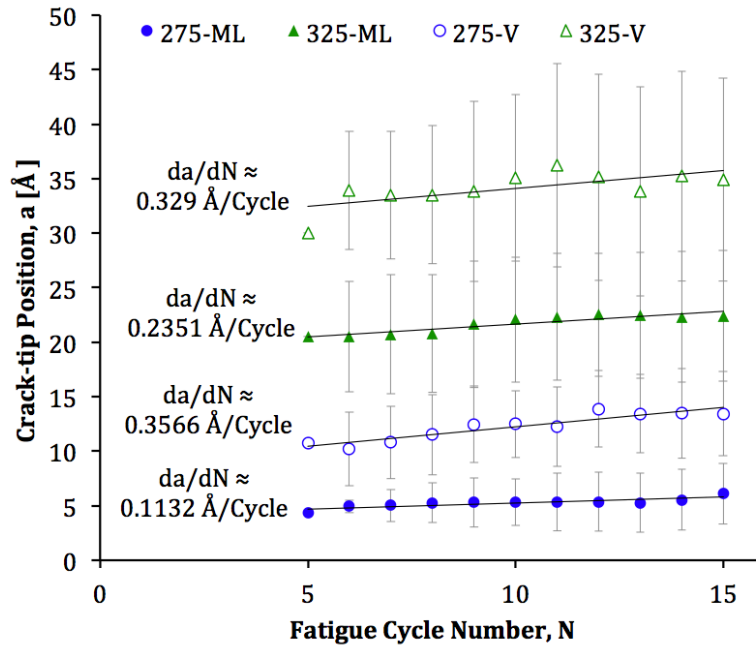


Figure 4.8: Although the average crack-growth distances observed within the first five loading cycles range from about 1-6 Å/cycle depending on the specific load range and presence of a surface film, the crack-growth rates slow dramatically as the loading progresses. Nevertheless, the approximate growth rates determined from a linear fit predict increased $\frac{da}{dN}$ in a vacuum environment. Error bars depict half the standard deviation distance in each direction.

were utilized (\approx 15-20 nm). This detail limited the loads available for consideration in the current work.

In addition to highlighting the need for large or adaptive atomistic domains, the current work also suggests that the long-term growth mechanism of near-threshold cracks in zero-temperature conditions may be the gradual reordering of quasi-stable defect structures ahead of the crack-tip. In the simulations performed here, these defect structures are comprised of dislocations that are immobile due to both elastic interactions as well as the limitations of periodic boundary conditions. Clearly, the use of out-of-plane periodic boundary condi-

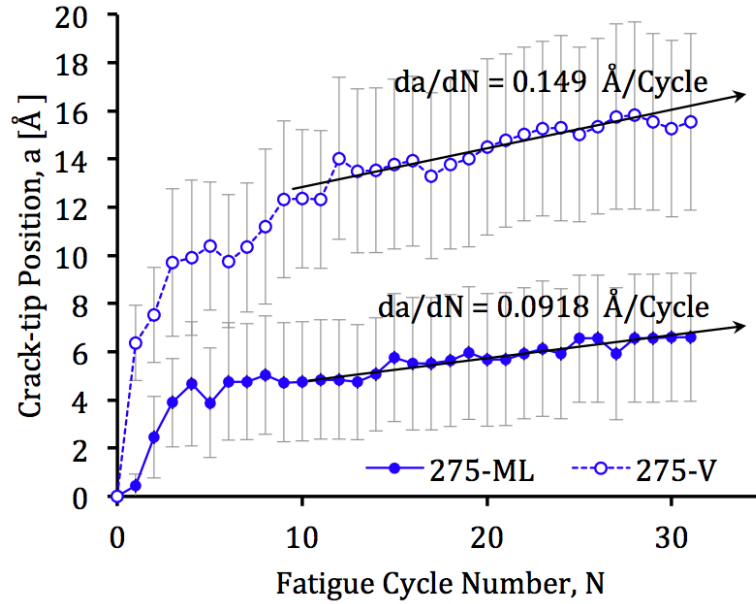


Figure 4.9: Plot of the average crack-tip position as a function of fatigue load cycle. Here, 32 load cycles were considered at $\Delta K = 0.275 \text{ eV}/\text{\AA}^{2.5}$ for both in-vacuo and surface-film conditions. Error bars depict half the standard deviation distance in each direction.

tions in the current model plays a strong role in the specific nature of the defect structures and dislocation character observed [2, 61]. However, the formation of immobile defects is a well-known occurrence [42, 40], and it is likely that the accommodation of high stress concentrations and shear-tension coupling present at a loaded crack-tip will enhance their formation. Therefore, ongoing development in the simulation of near-threshold fatigue behavior will likely require the development of models capable of capturing such immobile defect structures accurately. Such models should also consider the effects of temperature, as thermal fluctuations are likely to be an additional governing factor in the nucleation, glide and reordering of the underlying dislocations.

Regarding the effects of monolayer surface stiffening on crack-tip deformation behavior. This detail was found to be clearly inhibitive of both dislocation

nucleation and the overall near-threshold propagation of fatigue cracks. Although it seems intuitive that the stiffening of bonds is likely to inhibit any form of failure, several oxide-based mechanisms have been proposed for the acceleration of fatigue crack growth [21]. For example, it is believed that the formation of an oxide film during the loading stage of a fatigue cycle can encourage crack growth by preventing both slip-reversal and crack-face re-welding during the unloading stage. The results presented here suggest that this is not a probable mechanism at near threshold loads, because the ability for a surface to nucleate dislocations and experience interatomic decohesion seems to play a more critical role in the growth a fatigue crack than does the reversibility of slip.

It is possible that the experimentally observed acceleration of near-threshold fatigue growth rates in dry-oxygen environments is a result of surface film-based mechanisms beyond the reach of the model used here [21, 54, 55]. However, the clearly inhibitive results observed during direct simulation suggest that any acceleration is likely due to the well-established embrittling effects of aluminum-water interactions and the resulting presence of elemental hydrogen impurities [44, 45, 59, 14]. Even in a dry-oxygen environment, it is likely that trace levels of highly mobile [60, 62] hydrogen will have time to diffuse to the crack-tip during slow near-threshold growth. In this case, the presence of a stiff oxide film is likely to enhance the embrittling effects of hydrogen by preventing crack-tip blunting, and further localizing the fatigue process zone. This possibility is consistent with the experimental observation of reduced crack-tip blunting in laboratory air compared to vacuum [44, 6].

Overall, the work presented here makes significant progress in an ongoing effort to illuminate the micro-mechanical origins of near-threshold fatigue crack

growth in aluminum alloys. Although a number of critical limitations remain, the current methodologies have provided useful insights for the design and implementation of future models.

4.7 Summary and Conclusions

We have utilized a concurrently coupled atomistic and discrete dislocation multiscale method to directly simulate crack-tip deformation and propagation during near-threshold fatigue loading in aluminum. For the single crystal orientation considered, deformation behavior was generally found to begin with a short period of fast transient crack-tip propagation that slows once a quasi-stable defect structure has accumulated ahead of the crack-tip. Beyond the transient propagation stage, slow and irregular crack-growth behavior was observed. The approximate effects of monolayer surface stiffening were found to clearly inhibit crack growth by resisting initial slip-plane cracking behavior and the restructuring of defects ahead of the crack-tip surface.

In light of the results presented here, it is clear that fatigue behavior must be studied within very large or adaptive atomistic modeling domains. Furthermore, the limitations imposed by periodic boundary conditions and low-temperature approximations must be addressed. Given that the primary mechanism observed here for fatigue crack growth is the restructuring of trapped quasi-stable defects, it is critical that future models are capable of determining the true nature of these factors.

CHAPTER 5

CONCLUSION

In summary, three papers have been presented with the common goal of illuminating the atomistic-scale mechanisms governing environmentally assisted fatigue. In the second chapter, entitled “Ab-initio prediction of environmental embrittlement at a crack tip in aluminum,” an ab-initio atomistic-continuum multiscale framework was used to directly simulate dislocation nucleation at a loaded crack tip in the presence of elemental oxygen and hydrogen impurities. Results of the multiscale simulations and subsequent analysis were in support of the notion that electronegative surface impurities can inhibit dislocation nucleation from a crack-tip, which is consistent with macroscopic brittle failure.

In the third chapter, entitled “Illuminating the chemo-mechanics of hydrogen enhanced fatigue crack growth in aluminum alloys,” a series of computational studies were used to directly link an atomistic mechanism of hydrogen assisted cracking (HAC) to experimental fatigue data. The study began with an ab-initio investigation into the effects of hydrogen bonding on slip and decohesion at a $\{111\}$ aluminum surface, and was followed by the formulation of an approximate implicit hydrogen model. Finally, this implicit model was used within a coupled atomistic-continuum discrete dislocation framework to predict the effect of hydrogen on near threshold fatigue crack growth rates. The predicted trends were in agreement with published experimental data, suggesting that hydrogen enhanced surface deformation is a key failure mechanism for aluminum alloys in humid environments.

In the fourth chapter, entitled “Near-threshold fatigue loading in aluminum and the mechanical effects of monolayer surface-layer stiffening,” a modified

coupled atomistic and discrete dislocation (CADD) model was used to directly simulate crack-tip deformation and propagation during near-threshold fatigue loading in aluminum. The presence of environmental surface stiffening was approximated through the addition of a Lennard-Jones overlay potential. The results exhibited three general trends. First, fatigue behavior commenced with a short period of fast transient crack-tip propagation lasting between one and five load cycles. This period of fast propagation generally slowed once a stable defect structure had accumulated ahead of the crack-tip. Second, within each isolated fatigue simulation, crack growth was highly irregular and discontinuous. Third, the approximate effects of surface stiffening resulted in the inhibition of both dislocation nucleation and overall crack growth rates.

Altogether, the presented papers have further illuminated the atomistic level mechanisms governing near-threshold fatigue by quantifying the effects of specific environmental impurities on specific deformation mechanisms. Although there are many remaining questions regarding the true nature of near-threshold fatigue in aluminum, this work has clarified some of the specific modeling limitations that need to be overcome before these questions can be answered.

BIBLIOGRAPHY

- [1] S. Aubry, K. Kang, S. Ryu, and W. Cai. Energy barrier for homogeneous dislocation nucleation: Comparing atomistic and continuum models. *Scripta Materialia*, 64(11):1043 – 1046, 2011.
- [2] K. L. Baker and D. H. Warner. An atomistic investigation into the nature of near threshold fatigue crack growth in aluminum alloys. *Engineering Fracture Mechanics*, 115(0):111 – 121, 2014.
- [3] C. D. Beachem. A new model for hydrogen-assisted cracking (hydrogen embrittlement). *Metallurgical Transactions*, 3(2):441–455, 1972.
- [4] N. Bernstein, J. R. Kermode, and G. Csanyi. Hybrid atomistic simulation methods for materials systems. *Reports on Progress in Physics*, 72(2), 2009.
- [5] A. Bonakdar, F. Wang, J. J. Williams, and N. Chawla. Environmental effects on fatigue crack growth in 7075 aluminum alloy. *Metallurgical and Materials Transactions A*, 43(8):2799–2809, 2012.
- [6] F. J. Bradshaw and C. Wheeler. The influence of gaseous environment and fatigue frequency on the growth of fatigue cracks in some aluminum alloys. *International Journal of Fracture Mechanics*, 5(4):255–268, 1969.
- [7] M. Creager and P. C. Paris. Elastic field equations for blunt cracks with reference to stress corrosion cracking. *International Journal of Fracture*, 3:247–252, 1967.
- [8] W. A. Curtin and R. E. Miller. Atomistic/continuum coupling in computational materials science. *Modelling and Simulation in Materials Science and Engineering*, 11(3):R33, 2003.
- [9] M. S. Daw and M. I. Baskes. Embedded-atom method: Derivation and application to impurities, surfaces, and other defects in metals. *Physical Review B*, 29:6443–6453, Jun 1984.
- [10] V. S. Deshpande, A. Needleman, and E. Van der Giessen. A discrete dislocation analysis of near-threshold fatigue crack growth. *Acta Materialia*, 49(16):3189 – 3203, 2001.
- [11] F. Ercolessi and J. B. Adams. Interatomic potentials from 1st-principles

- calculations - the force-matching method. *Europhysics Letters*, 26(8):583–588, 1994.
- [12] D. Farkas, M. Duranduru, W. A. Curtin, and C. Ribbens. Multiple-dislocation emission from the crack tip in the ductile fracture of al. *Philosophical Magazine A*, 81(5):1241–1255, 2001.
- [13] D. Farkas, M. Willemann, and B. Hyde. Atomistic mechanisms of fatigue in nanocrystalline metals. *Physical Review Letters*, 94:165502, Apr 2005.
- [14] M.F. Francis. PhD thesis, University of Virginia, 2011.
- [15] R. P. Gangloff and B. P. Somerday. *Gaseous Hydrogen Embrittlement of Materials in Energy Technologies: Volume 1: The Problem, Its Characterisation and Effects on Particular Alloy Classes*. Woodhead Publishing, 2012.
- [16] Bray G. H., Bucci R. J., Brazill R. L., Starke E. A., Sanders T. H., and Casada W. A. Lessons neglected: Effects of moist air on fatigue and fatigue crack growth in aluminum alloys. *Materials science forum*, 331-337(7):1413–1426, 2000.
- [17] M. F. Horstemeyer, D. Farkas, S. Kim, T. Tang, and G. Potirniche. Nanostructurally small cracks (nsc): A review on atomistic modeling of fatigue. *International Journal of Fatigue*, 32(9):1473 – 1502, 2010.
- [18] L. Hung and E. A. Carter. Ductile processes at aluminium crack tips: comparison of orbital-free density functional theory with classical potential predictions. *Modelling and Simulation in Materials Science and Engineering*, 19(4):045002, 2011.
- [19] D. E. Jiang and E. A. Carter. First principles assessment of ideal fracture energies of materials with mobile impurities: implications for hydrogen embrittlement of metals. *Acta Materialia*, 52(16):4801 – 4807, 2004.
- [20] J. E. Jones. On the determination of molecular fields. ii. from the equation of state of a gas. *Proceedings of the Royal Society of London. Series A, Containing Papers of a Mathematical and Physical Character*, pages 463–477, 1924.
- [21] J. E. King. Role of oxides in fatigue crack propagation. *Materials Science and Technology*, 6(1):19–31, 1990.

- [22] W. Kohn and L. J. Sham. Self-consistent equations including exchange and correlation effects. *Physical Review*, 140:A1133–A1138, Nov 1965.
- [23] G. Kresse and J. Hafner. Ab-initio molecular dynamics for open shells transition-metals. *Phys. Rev. B*, 48(17):13115–13118, 1993.
- [24] G. Kresse and J. Hafner. Norm-conserving and ultrasoft pseudopotentials for first-row and transition-elements. *Journal of Physics-Condensed Matter*, 6(40):8245–8257, 1994.
- [25] C. Lanthony, J. M. Ducere, M. D. Rouhani, A. Hemeryck, A. Estve, and C. Rossi. On the early stage of aluminum oxidation: An extraction mechanism via oxygen cooperation. *The Journal of Chemical Physics*, 137(9):–, 2012.
- [26] Y. Liang, P. Sofronis, and N. Aravas. On the effect of hydrogen on plastic instabilities in metals. *Acta Materialia*, 51(9):2717 – 2730, 2003.
- [27] G. Lu, D. Orlikowski, I. Park, O. Politano, and E. Kaxiras. Energetics of hydrogen impurities in aluminum and their effect on mechanical properties. *Physical Review B*, 65(6):9, 2001.
- [28] S. P. Lynch. Environmentally assisted cracking: Overview of evidence for an adsorption-induced localised-slip process. *Acta Metallurgica*, 36(10):2639 – 2661, 1988.
- [29] S. P. Lynch. Metallographic contributions to understanding mechanisms of environmentally assisted cracking. *Metallography*, 23(2):147 – 171, 1989.
- [30] M. Methfessel and A. T. Paxton. High-precision sampling for Brillouin-zone integration in metals. *Physical Review B*, 40(6):3616–3621, 1989.
- [31] K. Momma and F. Izumi. VESTA: a three-dimensional visualization system for electronic and structural analysis. *Journal of Applied Crystallography*, 41(3):653–658, Jun 2008.
- [32] J. G. Morlet, H. H. Johnson, and A. R. Troiano. *A new concept of hydrogen embrittlement in steel*. WADC technical report. Wright Air Development Center, Air Research and Development Command, United States Air Force, 1957.
- [33] A. K. Nair, D. H. Warner, and R. G. Hennig. Coupled quantumcontinuum

- analysis of crack tip processes in aluminum. *Journal of the Mechanics and Physics of Solids*, 59(12):2476 – 2487, 2011.
- [34] A. K. Nair, D. H. Warner, R. G. Hennig, and W. A. Curtin. Coupling quantum and continuum scales to predict crack tip dislocation nucleation. *Scripta Materialia*, 63(12):1212 – 1215, 2010.
- [35] S. Ogata, F. Shimojo, R. K. Kalia, A. Nakano, and P. Vashishta. Environmental effects of H₂O on fracture initiation in silicon: A hybrid electronic-density-functional/molecular-dynamics study. *Journal of Applied Physics*, 95(10):5316–5323, MAY 15 2004.
- [36] R. A. Oriani. A mechanistic theory of hydrogen embrittlement of steels. *Berichte der Bunsengesellschaft fr physikalische Chemie*, 76(8):848–857, 1972.
- [37] R. M. N. Pelloux. Crack extension by alternating shear. *Engineering Fracture Mechanics*, 1(4):697 – 704, 1970.
- [38] R. Pippan, C. Zelger, E. Gach, C. Bichler, and H. Weinhandl. On the mechanism of fatigue crack propagation in ductile metallic materials. *Fatigue and Fracture of Engineering Materials and Structures*, 34(1):1–16, 2011.
- [39] S. Plimpton. Fast parallel algorithms for short-range molecular dynamics. *Journal of Computational Physics*, 117(1):1 – 19, 1995.
- [40] J. R. Rice. The mechanics of crack tip deformation and extension by fatigue. *fatigue crack propagation*, ASTM, ASTM STP, page 415, 1966.
- [41] J. R. Rice. Dislocation nucleation from a crack tip. an analysis based on the peierls concept. *Journal of the Mechanics and Physics of Solids*, 40(2):239–271, 1992.
- [42] F. O. Riemelmoser, R. Pippan, and H. P. Stuwe. A comparison of a discrete dislocation model and a continuous description of cyclic crack tip plasticity. *International Journal of Fracture*, 85(2):157–168, 1997.
- [43] R. O. Ritchie. Mechanisms of fatigue crack propagation in metals, ceramics and composites: role of crack tip shielding. *Materials Science and Engineering: A*, 103(1):15–28, 1988.
- [44] Y. Ro, S. R. Agnew, G. H. Bray, and R. P. Gangloff. Environment-exposure-

- dependent fatigue crack growth kinetics for al-cu-mg/li. *Materials Science and Engineering: A*, 468470(0):88 – 97, 2007.
- [45] Y. Ro, S. R. Agnew, and R. P. Gangloff. Effect of environment on fatigue crack wake dislocation structure in al-cu-mg. *Metallurgical and Materials Transactions A*, 43(7):2275–2292, 2012.
- [46] S. Serebrinsky, E. A. Carter, and M. Ortiz. A quantum-mechanically informed continuum model of hydrogen embrittlement. *Journal of the Mechanics and Physics of Solids*, 52(10):2403–2430, October 2004.
- [47] L. E. Shilkrot, R. E. Miller, and W. A. Curtin. Coupled atomistic and discrete dislocation plasticity. *Physical Review Letters*, 89:025501, Jun 2002.
- [48] L. E. Shilkrot, R. E. Miller, and W. A. Curtin. Multiscale plasticity modeling: coupled atomistics and discrete dislocation mechanics. *Journal of the Mechanics and Physics of Solids*, 52(4):755 – 787, 2004.
- [49] C. V. Singh and D. H. Warner. An Atomistic-Based Hierarchical Multiscale Examination of Age Hardening in an Al-Cu Alloy. *Metallurgical and Materials Transactions A*, 44:2625–2644, 2013.
- [50] P. Sofronis and I. M. Robertson. Transmission electron microscopy observations and micromechanical/continuum models for the effect of hydrogen on the mechanical behaviour of metals. *Philosophical Magazine A*, 82(17-18):3405–3413, 2002.
- [51] J. Song, M. Soare, and W. A. Curtin. Testing continuum concepts for hydrogen embrittlement in metals using atomistics. *Modelling and Simulation in Materials Science and Engineering*, 18(4):045003, 2010.
- [52] S.E. Stanzl, H.R. Mayer, and E.K. Tschegg. The influence of air humidity on near-threshold fatigue crack growth of 2024-t3 aluminum alloy. *Materials Science and Engineering: A*, 147(1):45 – 54, 1991.
- [53] Y. Sun, Q. Peng, and G. Lu. Quantum mechanical modeling of hydrogen assisted cracking in aluminum. *Physical Review B*, 88:104109, Sep 2013.
- [54] S. Suresh, I. G. Palmer, and R. E. Lewis. The effect of environment on fatigue crack growth behavior of 2021 aluminum alloy. *Fatigue and Fracture of Engineering Materials and Structures*, 5(2):133–150, 1982.

- [55] S. Suresh, A. K. Vasudvan, and P. E. Bretz. Mechanisms of slow fatigue crack growth in high strength aluminum alloys: Role of microstructure and environment. *Metallurgical Transactions A*, 15(2):369–379, 1984.
- [56] E. B. Tadmor and S. Hai. A peierls criterion for the onset of deformation twinning at a crack tip. *Journal of the Mechanics and Physics of Solids*, 51(5):765–793, 2003.
- [57] W. Tang, E. Sanville, and G. Henkelman. A grid-based bader analysis algorithm without lattice bias. *Journal of Physics: Condensed Matter*, 21(8):084204, 2009.
- [58] D. H. Warner, W. A. Curtin, and S. Qu. Rate dependence of crack-tip processes predicts twinning trends in f.c.c. metals. *Nature Materials*, 6(11):876–881, 2007.
- [59] R. P. Wei, P. S. Pao, R. G. Hart, T. W. Weir, and G. W. Simmons. Fracture mechanics and surface chemistry studies of fatigue crack growth in an aluminum alloy. *Metallurgical and Materials Transactions A*, 11(1):151–158, 1980.
- [60] C. Wolverton, V. Ozoliņš, and M. Asta. Hydrogen in aluminum: First-principles calculations of structure and thermodynamics. *Physical Review B*, 69:144109, Apr 2004.
- [61] V. I. Yamakov, D. H. Warner, R. J. Zamora, E. Saether, W. A. Curtin, and E. H. Glaessgen. Investigation of crack tip dislocation emission in aluminum using multiscale molecular dynamics simulation and continuum modeling. *Journal of the Mechanics and Physics of Solids*, 2014.
- [62] G. A. Young and J. R. Scully. The diffusion and trapping of hydrogen in high purity aluminum. *Acta Materialia*, 46(18):6337 – 6349, 1998.
- [63] R. J. Zamora, A. K. Nair, R. G. Hennig, and D. H. Warner. *Ab initio* prediction of environmental embrittlement at a crack tip in aluminum. *Physical Review B*, 86:060101, Aug 2012.